Research on Engineering Structures & Materials
www.jresm.org
Research Group

Research Article

Performance of geopolymer concrete flat slab with various transverse reinforcement in resisting punching shear

Siti Aisyah Nurjannah [*,a], Saloma [b], Arie Putra Usman [c], Faradiba [d]

Department of Civil Engineering, Universitas Sriwijaya, Indonesia

Article Info

Article History:

Received 23 Aug 2025

Accepted 31 Dec 2025

Keywords:

Concrete;
Finite element method;
Geopolymer;
Punching shear;
Reinforcement

Abstract

A flat slab is an efficient structure in resisting gravity loads by transferring the load from the slab to the columns and then to the foundations. Various normal concrete (NC) flat slab reinforcements against punching shear have been developed, including drop panels, steel plates, aluminum plates, additional longitudinal bar reinforcement, steel tubes, and transverse reinforcement. However, previous studies have not discussed the effect of the transverse reinforcement ratio that impacts capacity and ductility. In contrast, the performance of flat slabs with environmentally friendly concrete, such as geopolymer concrete (GC), has not been discussed. This study aims to analyze the performance of GC flat slabs reinforced with transverse reinforcement. The novelty of this study is extending the NC flat slab test results to GC flat slab numerical models with different transverse reinforcement. The performance of NC and GC flat slabs subjected to monotonic downward vertical loads is analyzed using a finite-element-based software. The issues discussed include shear load, deflection, stress contour, displacement contour, ductility, stiffness, energy absorption, and punching shear capacity. The results show that transverse reinforcement increases the flat slab capacity to withstand punching shear loads. The GC materials enhance shear strength. However, excessive transverse reinforcement results in brittle behavior and reduces deformation, ultimate load, and ultimate deflection.

1. Introduction

Geopolymer concrete is environmentally friendly because it does not contain Portland cement as a binder and its manufacturing process requires low energy [1,2], thereby supporting sustainable, environmentally friendly construction activities [3,4]. The binder during the hydration process in geopolymer concrete is a compound rich in silica and alumina, such as fly ash or rice husk ash [5,6,7], which is activated with alkaline liquid [8,9,10]. It supports reducing industrial and organic waste, which helps prevent climate change [2]. In contrast to geopolymer concrete, conventional concrete contains a binder—Portland cement —which produces carbon dioxide emissions [11], increases global temperatures [12], and creates pollution [13]. Geopolymer concrete has high durability [1,14,15], is more fire resistant than conventional concrete, and can be used as an insulator [16]. Geopolymer concrete has the potential to serve as a material for forming structural elements, as its mechanical properties can match or exceed those of conventional concrete. Geopolymer concrete achieves a compressive strength of 12.5-31.3 MPa [14], 28.5-50.1 MPa [6], and meets the minimum compressive strength requirements for structural elements of 17.5 MPa [17,18]. The interfacial shear capacity of geopolymer concrete ranges from 2.15 to 2.5 MPa [19], enabling it to form column and beam structural elements under axial and bending loads [20,21], as well as other structural elements, such as slabs and foundations. High-quality geopolymer concrete

*Corresponding author: sitiaisyahn@ft.unsri.ac.id
[a]orcid.org/0000-0003-3058-592X; [b]orcid.org/0000-0003-4302-0282; [c]orcid.org/0000-0002-1982-6561;
[d]orcid.org/0009-0009-5182-381X
DOI: http://dx.doi.org/10.17515/resm2026-1104me0823rs

reaches a compressive strength of 78.2-81.17 MPa [20], 163-210 MPa [21], and has the potential to be used as a material for forming structural elements that can withstand high compressive loads, namely foundations, bridge pillars, bridge girders, and prestressed beams [22,23].

Research on geopolymer concrete structural elements generally focuses on beams and columns to investigate their flexural and compressive performance [23-28]. The performance of flat slabs using geopolymer concrete materials and resisting punching shear loads has not been comprehensively studied and thus requires further investigation. Flat slab is one of the structural element systems for high-rise buildings that is vulnerable to seismic loads. Its function as a secondary seismic-resistant structure [29] makes it more suitable in the low-magnitude earthquake risk zones [30].

The corners of rectangular or square columns experience increased concrete strain concentrations as the ratio of the long to short sides of the column cross-section increases. The circular column cross-section reduces the concrete strain concentration and provides higher shear strength than rectangular columns [31]. The column shape affects the punching shear capacity of flat plates. The results of the analysis using the finite element method show that L-shaped, T-shaped, and Cross-shaped column cross-sections increase the punching shear capacity by 3%, 5.3%, and 22.6%, respectively, compared to columns with square cross-sections. This shows that the cross-sectional shape of the column can be effectively optimized to increase the punching shear resistance of flat plates [32].

The use of flat slabs reduces construction costs because they are built without beams. In the flat slab system, the concentrated axial load of the column is transferred directly to the flat slab and potentially causes damage due to punching shear. The performance of flat slabs in punching shear needs improvement. The transverse reinforcement system in flat slabs increases the shear capacity to withstand punching shear significantly [33-35].

Other methods for enhancing flat slab performance include shear reinforcement systems using diagonal and orthogonal aluminum sheets [36]. Aluminum sheets measuring 25 x 50 mm were installed at the mid-thickness of the slab to increase shear strength. The aluminum sheet installation position configurations were horizontal, vertical, diagonal, and hybrid. The aluminum sheet thicknesses were 1.0 mm, 1.5 mm, and 2.0-mm. Monotonic loading was gradually applied at a single location in the middle of the slab, downward until the specimen failed. The results of the investigation in this research showed that each aluminum sheet placement configuration slowed crack initiation and propagation. Aluminum sheets helped prevent the concrete cover from cracking before failure occurred. The thicker the aluminum sheet, the higher the initial cracking load in all aluminum sheet position configurations. The most significant increase in initial cracking load, 55.8%, was achieved with a flat slab using a combination of horizontal and vertical aluminum sheet configuration with a thickness of 2 mm. The most significant increase in ultimate load, 60.9%, was achieved with the flat slab reinforced with a hybrid aluminum sheet position. The highest increase in absorbed energy, 60%, was achieved by the flat slab with aluminum sheets in a combination of horizontal and vertical configurations.

Another type of reinforcement is a two-way integrity reinforcement, parallel to the column, located in the center of the flat slab and the compression zone [37]. Three flat slabs with a two-way ϕ8-60 longitudinal reinforcement were reinforced with integrity reinforcement installed in the X and Y axes in the center of the slab and the compression zone. The diameter variations for the three integrity reinforcements were 10 mm, 12 mm, and 14 mm for the flat slab types 1, 2, and 3, respectively. Each slab was also reinforced with perimeter reinforcement. The monotonic load was applied to the top of a short column in the middle of a rectangular steel plate as an intermediary. Before punching shear failure, concrete plays a more dominant role in resisting shear. Upon entering the punching shear condition, the concrete cracked and crushed; thus, the longitudinal steel reinforcement and integrity reinforcement were more dominant in resisting the load. Shear capacity increases with the larger diameter of the integrity reinforcement steel bar. The difference between the concrete compressive and steel tensile strengths significantly affected punching shear capacity and post-punching resistance.

Some other methods for improving flat slab performance are elaborated in the following brief reports. Reinforcement around concrete columns enclosed by steel tubes in the form of horizontal and vertical bearing plates enhances the performance of flat slabs in terms of punching shear capacity, ductility, and energy absorption. The gradually increasing vertical loading on the upper side of the column cross-section does not result in yielding of the horizontal bearing plates. Otherwise, the vertical bearing plates yield only at the upper and lower corners. This condition indicates that the vertical bearing plates provide a greater stiffness and contribute to resisting punching shear than the horizontal bearing plate. The use of larger vertical bearing plate dimensions or slab thickening increases resistance to punching shear. Another property of flat slabs that contributes to increased punching shear capacity is the concrete's compressive strength, which also increases ductility and energy absorption. The addition of tensile reinforcement significantly increases the punching shear capacity in flat slabs with minimal longitudinal reinforcement [38].

The use of steel plates at the column-to-flat slab connection has been shown to increase maximum load capacity and shear strength by up to 2.15 times. The rib plates connecting the column and the flat slab contribute to increased stiffness and shear performance. Some rib plates experienced premature buckling despite the application of rib plate thickening. The behavior of the flat slab reinforced with steel plates at the column-to-flat slab and rib plate connections is also influenced by the bond and deformation of the steel reinforcement [39].

The shear capacity of the flat slab-column connection was increased by using ultra-high-performance fiber-reinforced concrete material on the flat slab around the column with a side size of 273 mm to 600 mm in a square shape. High compressive strength in concrete increases the capacity of the flat slab-column connection in terms of initial stiffness, punching shear capacity, and deformation. The increase in capacity is influenced by the addition of a flat slab area with ultra-high-performance concrete containing fibers [40].

The above methods for improving flat slab performance indicate that punching shear resistance can be achieved by strengthening transverse reinforcement. The addition of shear reinforcement increases the maximum shear force that can be resisted by a flat slab in both elastic and inelastic conditions. Transverse reinforcement in thick slabs and waffle slabs can increase the shear capacity [41,42]. Thus, it can be applied to flat slabs to improve the ability to resist punching shear equivalent to or better than flat slabs with conventional concrete materials. However, research on the performance of flat slabs with geopolymer concrete materials and shear reinforcement to resist punching shear has not been comprehensively studied. An adequate transverse reinforcement provides sufficient shear capacity and enables geopolymer concrete flat slabs to resist punching shear.

This study aims to perform a performance analysis of geopolymer concrete flat slabs with transverse reinforcement to resist punching shear, with reinforcement of various diameters. The novelty of this study is extending the NC flat slab test results to the GC flat slab through numerical modeling with different transverse reinforcement configurations.

2. Materials and Methods

The research method involves investigating the mechanical properties of geopolymer concrete, including compressive strength, elastic modulus, and stress-strain relationship curves. The numerical modeling of a geopolymer concrete flat slab under monotonic loads was carried out using ANSYS, based on the finite element method, to analyze load-displacement relationships, stress and displacement contours, ductility, stiffness, energy absorption, and punching shear resistance. The transverse reinforcement was varied to investigate the flat slab's behavior in resisting punching shear under monotonic loading.

2.1. Details of Specimens and Models

In the previous research [41], the NC compressive strength and the modulus of elasticity were 30 MPa and 22500 MPa, respectively. The yield strength of steel for longitudinal reinforcement was 549 MPa for the flat slab without transverse steel reinforcement, and 615 MPa for the flat slab with

transverse reinforcement of ϕ5 and ϕ8. The yield strength of transverse reinforcement of ϕ5 and ϕ8 was 698 MPa and 706 MPa, respectively [41], as shown in Table 1. In all flat slab models, the upper longitudinal reinforcement was 16 mm in diameter, spaced at 155 mm, and connected with 16 mm hook-shaped rods at the same spacing. The lower longitudinal reinforcement diameter was 10 mm. The column reinforcement consisted of 8 longitudinal reinforcement bars with 16 mm in diameter surrounded by 10 mm in diameter stirrups with 80 mm spacing. The modeling analysis includes punching shear capacity, stress and displacement contours, ductility, strength degradation, and energy absorption [43-45].

The investigated flat slabs have dimensions of 2500 mm × 2500 mm with a thickness of 180 mm, effective depth of 162 mm, consisting of a composite of concrete and reinforcing steel. The concrete materials used in the specimens were normal concrete (NC), whereas in the numerical models, they were NC and geopolymer concrete (GC). The flexural reinforcement configuration from the previous research [41] is the same for all slabs. The upper longitudinal reinforcement has a diameter of 16 mm, spaced at 155 mm, and is connected with 16 mm-diameter steel bars in the form of hooks at the same spacing. The lower longitudinal reinforcement has a diameter of 10 mm and is placed directly below the upper reinforcing steel bars with a spacing of 155 mm. Table 1 shows the types of flat slabs. In the previous study [41], the NC flat slab specimens consisted of NC-0 and NC-5, while in this numerical study, the models consisted of three NC flat slab types (NC-0-F, NC-5-F, and NC-8-F) and three GC flat slab types (GC-0-F, GC-5-F, and GC-8-F). The NC-0 specimen and NC-0-F model do not have shear reinforcement. The NC-5 specimen and NC-5-F model were equipped with 5ϕ5 mm transverse reinforcement with 72 mm spacing, while the NC-8-F model used 5 ϕ8 mm with 72 mm spacing. The performance of the flat slab with increased transverse reinforcement area is analyzed in this study. The column cross-section is 300 mm × 300 mm, with 8D16 longitudinal reinforcement and ϕ8-80 stirrups. The clear column heights on the top and bottom sides of the flat slab are 800 mm and 600 mm, respectively. Details of the longitudinal and transverse steel bar reinforcements in all specimens [41], as well as the NC and GC models, are shown in Table 1. The GC compressive strength and elastic modulus are 41.5 MPa and 30266 MPa, respectively [46]. Details of the flat slab dimensions, longitudinal and transverse reinforcement from the top and side sections are shown in Figures 1 and 2, respectively. The reinforcement design for the flat slab to resist shear and bending, per code [17], is shown in Figure 3. Figure 4 shows the perimeter control, expressed as the dimensions and spacing of shear reinforcement, for the slab based on the code [17].

Table 1. Steel bars properties

Type of flat slab	Concrete material	Top and bottom longitudinal steel bar	Transverse steel bar	Transverse steel bar ratio	Longitudinal steel bar yield strength [41], f_{yl}	Transverse steel bar yield strength [41], f_{yt}
		(mm)	(mm)	(%)	(MPa)	(MPa)
NC-0 & NC-0-F	NC	ϕ16 & ϕ10	-	0	549	-
NC-5 & NC-5-F	NC	ϕ16 & ϕ10	ϕ5-72	0.17	615	698
NC-8-F	NC	ϕ16 & ϕ10	ϕ8-72	0.44	615	706
GC-0-F	GC	ϕ16 & ϕ10	-	0	549	-
GC-5-F	GC	ϕ16 & ϕ10	ϕ5-72	0.17	615	698
GC-8-F	GC	ϕ16 & ϕ10	ϕ8-72	0.44	615	706

In the experiment, a monotonic load was applied to the top of the column cross-section, which was covered with a steel plate serving as an intermediary between the horizontal loading frame and the column, as shown in Figure 5. The load cells pressed four spreader beams above the flat slab, resulting in uniform loads that caused the flat slab to move downwards. This condition persisted until the flat slab structure failed [41].

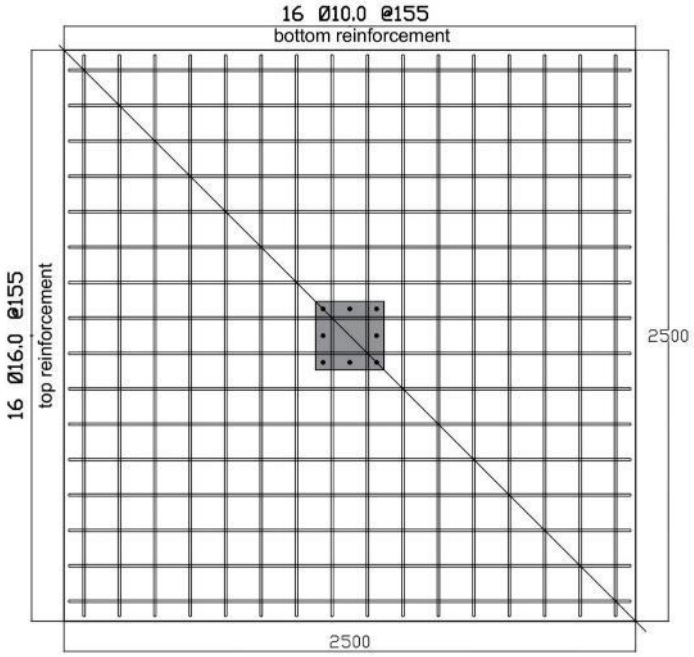

Fig. 1. Plan of flat slab details [41, redrawn]

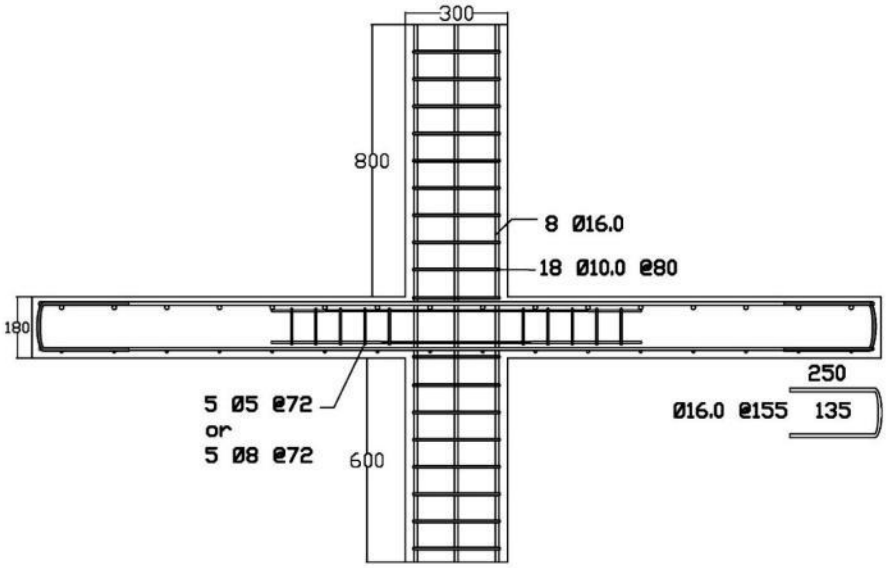

Fig. 2. Section of flat slab details [41, redrawn]

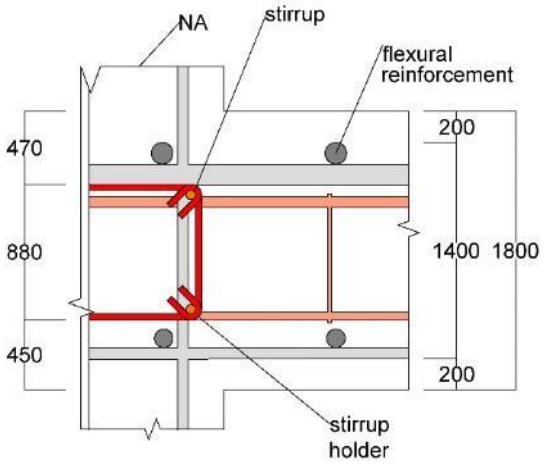

Fig. 3. Details of the transverse reinforcement [41, redrawn]

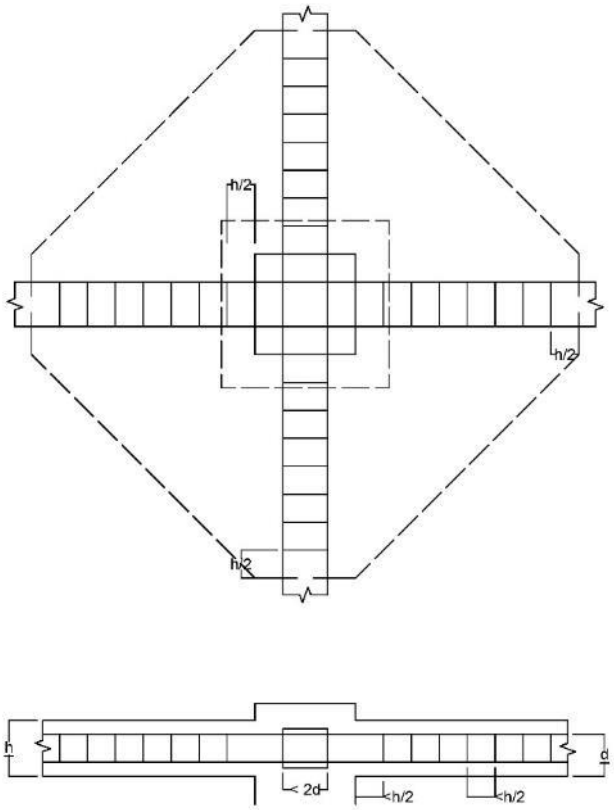

Fig. 4. Perimeter control and details for a flat slab [17, redrawn]

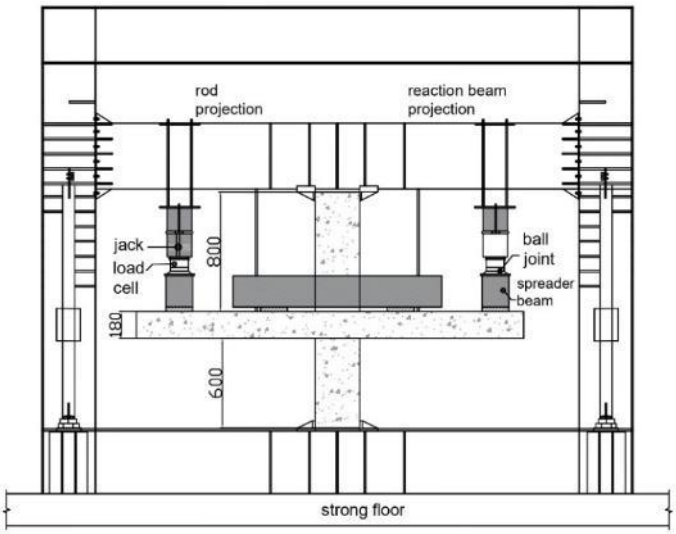

Fig. 5. Loading setup [41, redrawn]

2.2. Finite Element Modeling

The flat slab numerical model was developed using the finite element method under monotonic loading. The geometry, dimensions, details of the steel longitudinal and transverse reinforcement, concrete compressive strength, yield and ultimate strengths of the steel reinforcement, and monotonic loads were derived from previous research [41], as shown in Figure 1-5. Verification of the NC flat slab models was carried out by comparing the hysteretic curves of the load-displacement correlations from the numerical analysis with the experimental results of [41], with a tolerance of 10% to ensure accuracy [47,48].

The load-control method, with the exact loading location on the column and the spreader beams above the flat slab, was used in numerical modeling, where the compressive axial load was increased by 40 kN at each load step until failure. The position of the Linear Variable Differential

Transducer (LVDT) in the experiment [41], which became the reference for the flat slab displacement data in this study, was at a distance of 1050 mm from the center to the edge of the flat slab. The model for a flat slab and top-column structural system that supports uniform loads from four spreader beams and concentrated loads on the top of the column cross-section is shown in Figure 6. Figure 7 shows the flat slab structure connected to the columns. Flat slab finite element modeling was conducted by defining concrete and reinforcing steel as separate, discrete elements.

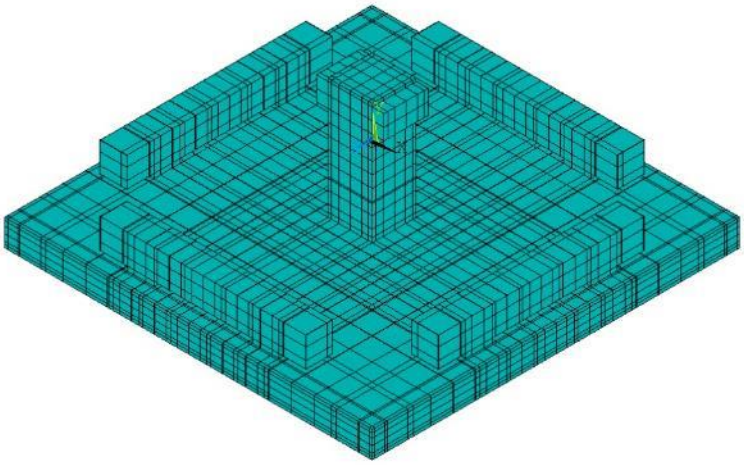

Fig. 6. The top side of a flat slab model

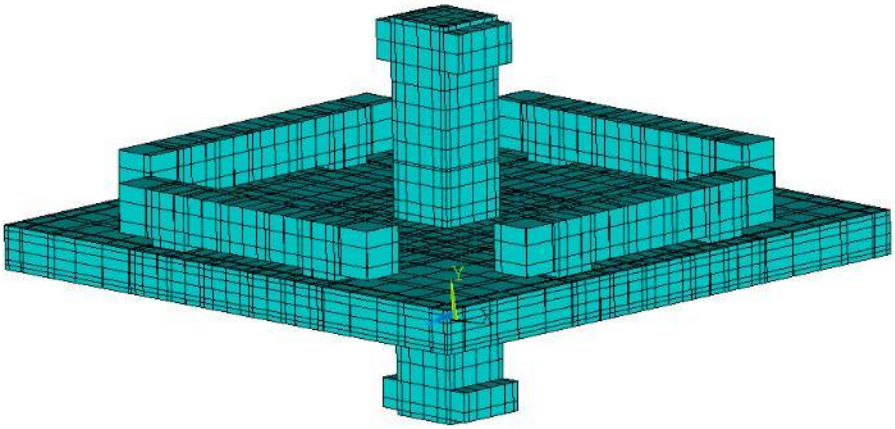

Fig. 7. Three-dimensional side view of the flat slab model

2.2.1 Concrete Element

The concrete is modeled using three-dimensional SOLID65 discrete elements with 8 nodes (8-node brick elements) in this study, as shown in Figure 8. Each node has three degrees of translational freedom in the X, Y, and Z axes. SOLID65 elements can be modeled as elements that experience cracking due to tensile stress, crushing due to compressive stress, plastic deformation, and creep.

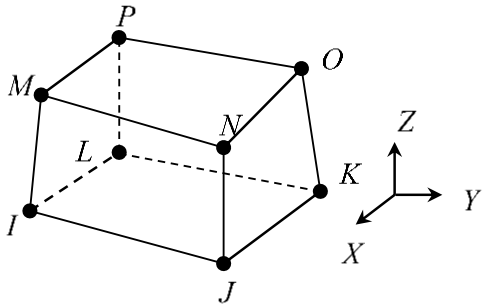

Fig. 8. SOLID65 element

2.2.1.1 Cracking Behavior of Concrete Elements

The material stiffness matrix under isotropic material conditions can be derived as in equation (1).

$$D^c = \frac{E}{(1+\upsilon)(1-2\upsilon)} \cdot \begin{bmatrix} (1-\upsilon) & \upsilon & \upsilon & 0 & 0 & 0 \\ \upsilon & (1-\upsilon) & \upsilon & 0 & 0 & 0 \\ \upsilon & \upsilon & (1-\upsilon) & 0 & 0 & 0 \\ 0 & 0 & 0 & \frac{(1-2\upsilon)}{2} & 0 & 0 \\ 0 & 0 & 0 & 0 & \frac{(1-2\upsilon)}{2} & 0 \\ 0 & 0 & 0 & 0 & 0 & \frac{(1-2\upsilon)}{2} \end{bmatrix} \quad (1)$$

Where; E: modulus of elasticity of concrete (MPa), υ : Poisson's ratio of concrete

The material stiffness from the stress-strain relationship for a cracked material in one direction is given by equation (2).

$$D_c^{ck} = \frac{E}{(1+\upsilon)} \begin{bmatrix} \frac{R^t(1-\upsilon)}{E} & \frac{\upsilon}{(1-\upsilon)} & \frac{\upsilon}{(1-\upsilon)} & 0 & 0 & 0 \\ 0 & \frac{1}{(1-\upsilon)} & \frac{\upsilon}{(1-\upsilon)} & 0 & 0 & 0 \\ 0 & \frac{\upsilon}{(1-\upsilon)} & \frac{1}{(1-\upsilon)} & 0 & 0 & 0 \\ 0 & 0 & 0 & \frac{\beta_t}{2} & 0 & 0 \\ 0 & 0 & 0 & 0 & \frac{1}{2} & 0 \\ 0 & 0 & 0 & 0 & 0 & \frac{\beta_t}{2} \end{bmatrix} \quad (2)$$

The notation ck represents the stress-strain relationship referring to a coordinate system parallel to the principal stress axis with the X^{ck} axis perpendicular to the crack plane. R^t is the slope (secant modulus) as in Figure 9. The notation f_t represents the tensile stress and T_c is the multiplier for tensile stress relaxation.

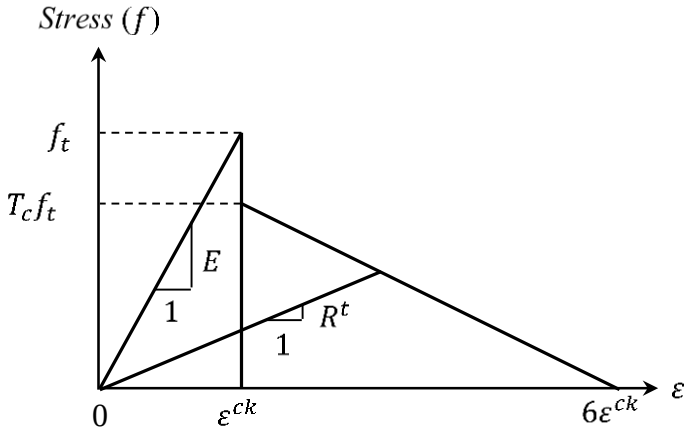

Fig. 9. Stress-strain diagram for cracked concrete material

Suppose the crack closes due to unloading conditions. In that case, the compressive stress perpendicular to the crack plane will be transferred to the crack, and there is only a shear transfer coefficient β_c, so that the stiffness matrix becomes as in equation (3).

$$D_c^{ck} = \frac{E}{(1+\upsilon)(1-2\upsilon)} \begin{bmatrix} (1-\upsilon) & \upsilon & \upsilon & 0 & 0 & 0 \\ \upsilon & (1-\upsilon) & \upsilon & 0 & 0 & 0 \\ \upsilon & \upsilon & (1-\upsilon) & 0 & 0 & 0 \\ 0 & 0 & 0 & \frac{\beta_c(1-2\upsilon)}{2} & 0 & 0 \\ 0 & 0 & 0 & 0 & \frac{\beta_c(1-2\upsilon)}{2} & 0 \\ 0 & 0 & 0 & 0 & 0 & \frac{\beta_c(1-2\upsilon)}{2} \end{bmatrix} \quad (3)$$

The stress-strain relationship for concrete that cracks in two directions is as in equation (4).

$$D_c^{ck} = E\begin{bmatrix} \frac{R^t}{E} & 0 & \upsilon & 0 & 0 & 0 \\ 0 & \frac{R^t}{E} & \upsilon & 0 & 0 & 0 \\ 0 & 0 & 1 & 0 & 0 & 0 \\ 0 & 0 & 0 & \frac{\beta_t}{2(1+\upsilon)} & 0 & 0 \\ 0 & 0 & 0 & 0 & \frac{\beta_t}{2(1+\upsilon)} & 0 \\ 0 & 0 & 0 & 0 & 0 & \frac{\beta_t}{2(1+\upsilon)} \end{bmatrix} \quad (4)$$

If the crack closes in two directions, then the stress-strain relationship is as in equation (3). The stress-strain relationship of concrete cracked in three directions is in accordance with equation (4). If the crack closes in three directions, then the stress-strain relationship is as in equation (3). The state of the crack is open or closed, depending on the strain value ε_{ck}^{ck}, which is called the crack strain. For the condition of the crack in the X-axis direction, the strain value is obtained by equation (5).

$$\varepsilon_{ck}^{ck} = \begin{cases} \varepsilon_X^{ck} + \frac{\upsilon}{1-\upsilon}\varepsilon_Y^{ck} + \varepsilon_Z^{ck} & \text{if no crack occurs} \\ \varepsilon_Y^{ck} + \upsilon\varepsilon_Z^{ck} & \text{if the crack is in the Y-axis direction} \\ \varepsilon_X^{ck} & \text{if the crack is in the Y and Z axis direction} \end{cases} \quad (5)$$

where $\varepsilon_X^{ck}, \varepsilon_Y^{ck}, \varepsilon_Z^{ck}$ are the three components of normal strain in the crack direction.

If ε_{ck}^{ck} is less than zero, then the crack is assumed to be closed, whereas if ε_{ck}^{ck} is equal to or greater than zero, then the crack is assumed to be open. When the first crack occurs, the crack is assumed to be open for the next iteration.

2.2.1.2 Concrete Destruction Behavior and Damage Criteria

If a material is crushed by uniaxial, biaxial, or triaxial compressive forces, it is considered to be crushed. In the SOLID65 element in ANSYS, if crushing occurs, the material's stiffness contribution can be ignored. Concrete material that undergoes cracking and deterioration is modeled using the CONC type in SOLID65 elements. The failure criteria resulting from multiaxial stress are given by equation (6).

$$\frac{F}{f_c} - S \geq 0 \quad (6)$$

Where; F: a symbol to state the principal stress; S: failure area expressed in terms of principal stress and five parameters (f_t, f_c, f_{cb}, f_1, and f_2); σ_{xp}, σ_{yp}, σ_{zp}: principal stresses in the direction of the principal axis; f_t : ultimate uniaxial tensile strength (MPa); f_c: Ultimate uniaxial compressive strength (MPa); f_{cb}: Ultimate biaxial compressive strength (MPa); f_1: Ultimate biaxial compressive strength plus hydrostatic stress (MPa); f_2: Ultimate uniaxial compressive strength plus hydrostatic stress (MPa).

The behavior of concrete material is modeled using Multilinear Isotropic Hardening (MISO) in the ANSYS software, as shown in Fig. 10. MISO uses the von Mises yield criterion and isotropic work hardening. The slope of the first segment of the curve (initial slope) represents the material's modulus of elasticity. Subsequent slopes must be greater than zero and less than the elastic modulus. The stress-strain curve can be defined up to 100 points. The response of concrete under loading is determined by its nonlinear behavior. Typical stress-strain behavior of concrete subjected to uniaxial loading is shown in Fig. 11.

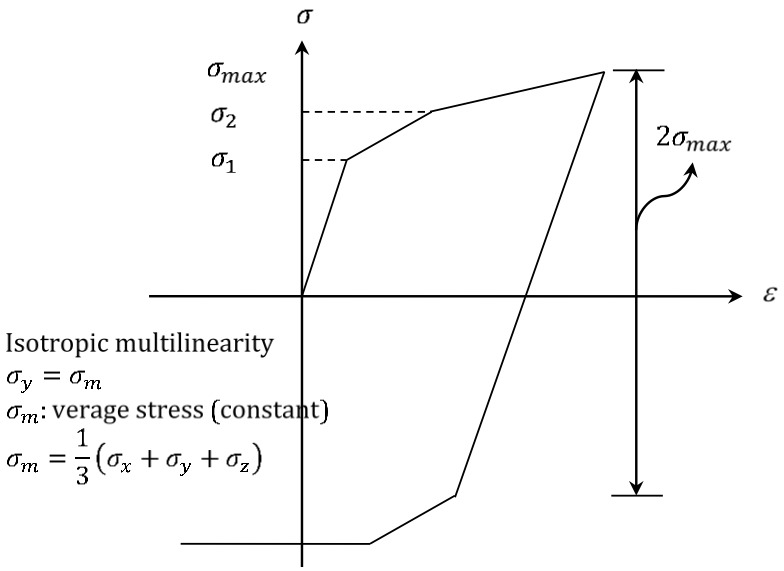

Fig. 10. Isotropic multilinear stress-strain diagram [49]

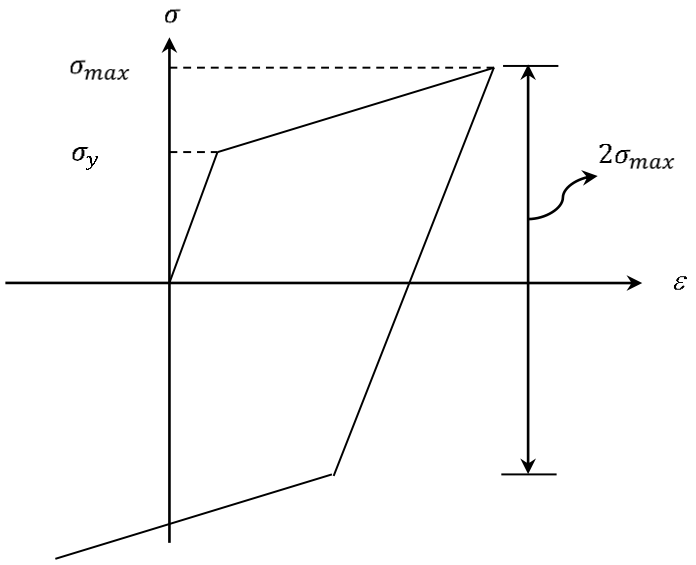

Fig. 11. Kinematic bilinear stress-strain diagram [49]

2.2.2 Steel Bar Element

In this study, the longitudinal and transverse reinforcing steel element models use 2-nodes LINK180 discrete bar elements in the ANSYS software. The axial forces at the ends of the LINK180 bars are as shown in Figure 12. The reinforcing steel is assumed to be fully bonded to the concrete.

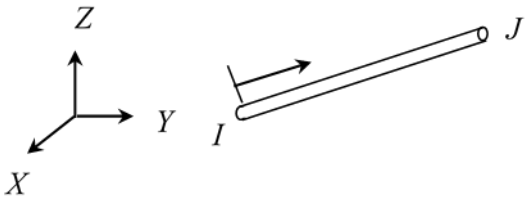

Fig. 12. LINK180 element

In these models, the element is formed through two points at the ends of the bar in the Cartesian coordinate system X, Y, Z. Each point has three degrees of freedom in the form of translations along the X, Y, and Z axes. The element does not experience bending, and the stresses are assumed to be

the same along the length of the element bar. The element stiffness matrix is expressed in equation (7), where A is the cross-sectional area of the element (mm^2), E_s is the modulus of elasticity of the steel (MPa), and L is the length of the element (mm). Multilinear Kinematic Hardening (MKIN) is used for reinforcing elements. In MKIN, the Bauschinger effect is assumed, with the total stress equal to twice the yield stress. The initial slope of the curve represents the material's elastic modulus, which is greater than zero. Subsequent slopes must be less than the elastic modulus.

$$[K] = \frac{AE_s}{L}\begin{bmatrix} 1 & 0 & 0 & -1 & 0 & 0 \\ 0 & 0 & 0 & 0 & 0 & 0 \\ 0 & 0 & 0 & 0 & 0 & 0 \\ -1 & 0 & 0 & 1 & 0 & 0 \\ 0 & 0 & 0 & 0 & 0 & 0 \\ 0 & 0 & 0 & 0 & 0 & 0 \end{bmatrix} \tag{7}$$

2.2.3 Boundary Conditions and Load

The flat slab model created in ANSYS software is identical to the specimen used in the experimental testing reported in previous research [41]. In the model, the width of the flat slab and column is in the x-axis direction, the height of the flat slab is in the y-axis direction, and the thickness of the flat slab is in the z-axis direction. In the flat slab specimen, clamps are placed to prevent the structural members from moving during testing. The middle of the column on the flat slab is given a concentrated downward load of $0.1f_c'A_g$. The top of the flat slab is provided with four spreader beams and four flexible hydraulic actuators that can move up and down. Each flat slab model has supports and loads at the exact locations as the specimen to ensure precise boundary conditions.

Monotonic loads are applied by four hydraulic actuators that press eight steel plates at the top ends of the four spreader beams. The load is then transferred from the spreader beams to the flat slab. The top of the columns is loaded through steel plates with the same load increment as the spreader beams [41]. In the numerical models, monotonic loads are applied to the top of each left and right end of the four spreader beams and the top of the columns.

2.2.4 Nonlinear Solving Solution

The solution of nonlinear equations satisfying boundary conditions using the finite element method in ANSYS software can be described as follows. When the stress-strain relationship for concrete and reinforcing steel elements is nonlinear, a solution to the nonlinear equations is required. In the structural plane, equation (8) is for linear systems.

$$[K]\{u\} = \{F^a\} \tag{8}$$

Where; $[K]$: structural stiffness matrix; $\{u\}$: degrees of freedom vector; $\{F^a\}$: load vector.

Equation (9) needs to be modified to satisfy the boundary conditions in nonlinear cases. An iterative process is required to obtain a solution to the equation. ANSYS provides some methods to solve nonlinear equations, including the Newton-Raphson method [50]. An iterative process of this method is applied to solve the nonlinear equations (9) and (10).

$$\left[K_i^T\right]\{\Delta u_i\} = \{F^a\} - \{F_i^{nr}\} \tag{9}$$

$$\{u_{i+1}\} = \{u_i\} + \{\Delta u_i\} \tag{10}$$

Where; $[K_i^T]$: structural stiffness matrix; $\{u_i\}$: degrees of freedom vector; $\{F_i^{nr}\}$: load vector

Iterations are required to obtain a convergent solution with the following workflow:

- Assume the value of $\{u_o\}$. The $\{u_o\}$ is the solution of the previous iteration step. Thus, in the first iteration, $\{u_o\}$ = {0}.
- Obtain $[K_i^T]$, with $\{F_i^{nr}\}$ is from $\{u_i\}$ confirmation.

- Obtain $\{\Delta u_i\}$.
- Add $\{\Delta u_i\}$ to $\{u_i\}$ to obtain $\{u_{i+1}\}$

Figure 13 shows the next iteration process to solve a nonlinear equation. It provides a solution of the iteration process when the load factor $\{F_i^{nr}\}$ is equal to $\{F\}$, or less than a specific tolerance value of 0.001. In this study, the Full Newton-Raphson method was chosen for solving iterations using an ANSYS software, which built the initial stiffness matrix in each iteration.

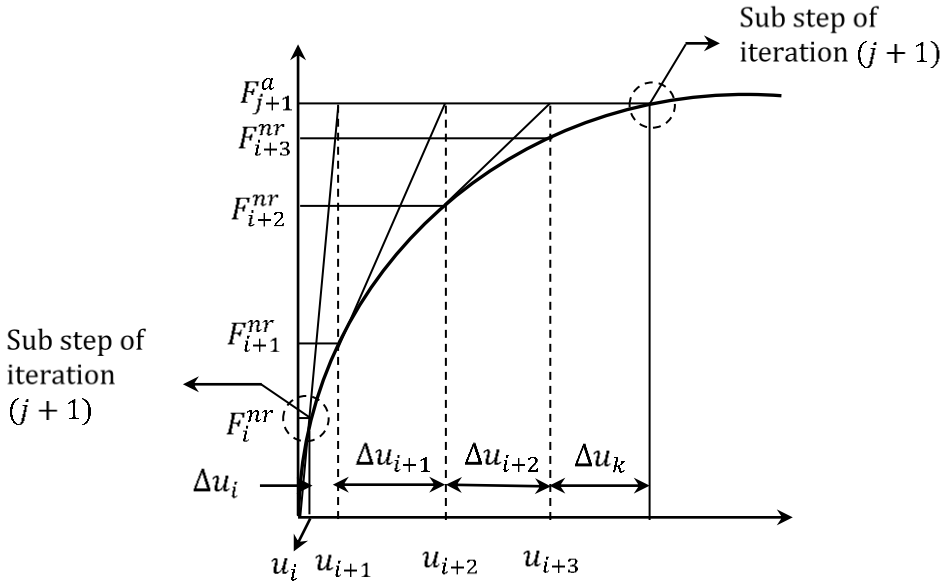

Fig. 13. Newton-Raphson iteration on one loading sub-step

2.3. Material Properties

In numerical modeling, the stress-strain relationship was based on the Hognestad equation, which has been shown to best match test results for NC and GC materials compared to other equations [51]. Equations (11) and (12) represents the stress-strain relationship according to Hognestad in ascending and descending curves, respectively. The tensile strengths of NC and GC are obtained from equation (13) [17], which yields tensile strengths closest to the test results for NC and GC [51]. The Poisson's ratios of NC and GC are assumed to be 0.2 [52] and 0.22 [53], respectively. For comparison, other equations of stress-strain in ascending and descending curves referring to Kent-Park, Saatcioglu-Razvi, and Mander are stated in equations (14-19). The Hognestad stress-strain curve is not much different compared to the Kent-Park, Saatcioglu-Razvi, and Mander curves in Figure 14.

$$f_c = f_c' \left[2\left(\frac{\varepsilon_c}{\varepsilon_o}\right) - \left(\frac{\varepsilon_c}{\varepsilon_o}\right)^2\right] \text{ (Hognestad; ascending)} \quad (11)$$

$$f_c = 0.85\, f_c' \text{ (Hognestad; descending)} \quad (12)$$

$$f_s = 0.33\sqrt{f_c'} \quad (13)$$

$$f_c = f_c' \left[2\left(\frac{\varepsilon_c}{\varepsilon_o}\right) - \left(\frac{\varepsilon_c}{\varepsilon_o}\right)^2\right] \text{ (Kent-Park; ascending)} \quad (14)$$

$$f_c = f_c'[1 - 100(\varepsilon_c - 0.002)] \text{ (Kent-Park; descending)} \quad (15)$$

$$f_c = f_c' \left[2\left(\frac{\varepsilon_c}{\varepsilon_o}\right) - \left(\frac{\varepsilon_c}{\varepsilon_o}\right)^2\right] \text{ (Saatcioglu-Razvi; ascending)} \quad (16)$$

$$f_c = f_c' + \left[\frac{f_c' - f_{c85}}{\varepsilon_{co} - \varepsilon_{c85}}\right](\varepsilon_c - \varepsilon_{co}) \text{ (Saatcioglu-Razvi; descending)} \quad (17)$$

$$f_c = \frac{f_c' xr}{r - 1 + x^r} \text{ (Mander; ascending and descending)} \quad (18)$$

$$x = \frac{\varepsilon_c}{\varepsilon_{co}};\ r = \frac{E_c}{E_c - E_{sec}};\ E_c = 5000\sqrt{f_c'};\ E_{sec} = \frac{f_c'}{\varepsilon_{co}} \text{ (Mander)} \quad (19)$$

Where; $\boldsymbol{\varepsilon_o}$: concrete compressive strain at ultimate stress = 0.002; $\boldsymbol{f_c}$: concrete compressive stress (MPa); $\boldsymbol{f_c'}$: uniaxial compressive strength (MPa); $\boldsymbol{f_{c85}}$: 85% of uniaxial compressive strength (MPa); $\boldsymbol{E_c}$: modulus of elasticity of concrete (MPa); $\boldsymbol{f_s}$: tensile strength of concrete (MPa)

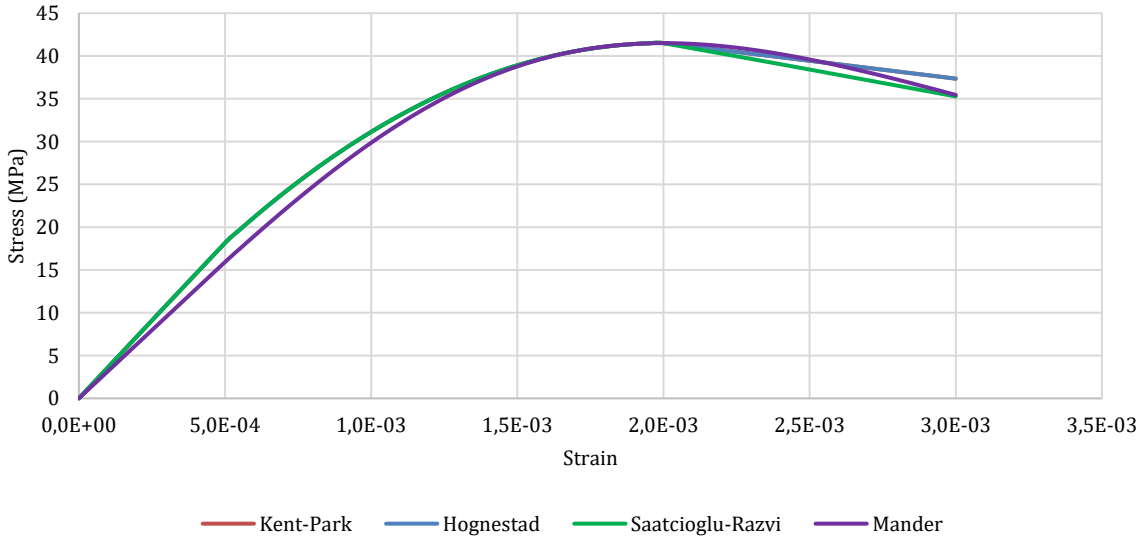

Fig. 14. GC stress-strain curves with Kent-Park, Hognestad, Saatcioglu-Razvi, and Mander equations

The fracture energy is expressed in equation (20) [35]. The maximum diameter of aggregates was 16 mm for NC [41] and 4.75 mm for GC [46]. The initial fracture energy for NC is 0.03 N/mm and 0.025 N/mm for GC [54]. Then, the fracture energies for NC and GC are 64.73 N/mm^2 and 67.70 N/mm^2, respectively.

$$G_f = G_{f0}[(f_c'/10)^{0.7}] \quad (20)$$

Where; G_f: fracture energy of concrete (N.m/mm2); G_{f0}: initial fracture energy (N/mm)

3. Results and Discussion

The load-displacement relationship curve is influenced by transverse reinforcement. The model loading process is the same as the experiment, namely by increasing the gravity load on the spreader beams in 40 kN increments [41]. Comparison of the experimental load-displacement relationship curves and flat slab-column modeling of NC-0, NC-0-F, NC-5, and NC-5-F is shown in Figure 14. The NC-0, NC-0-F, NC-5, and NC-5-F load-displacement curves almost match, due to the overlapping curves resulting from nearly the same slopes and stiffnesses. The difference in load and displacement at the initial and ultimate loading conditions is less than 10% as stated in Table 2. It indicates the accuracy of the modeling [47,48]. The highest punching shear capacity is achieved by the NC-8-F, followed by NC-5, NC-5-F, and NC-0, NC-0-F. The transverse reinforcement ratio

affects the punching shear capacity and deformability [55]. Without transverse reinforcement, NC-0 and NC-0-F cannot achieve vertical displacements as far as NC-5, NC-5-F, NC-8, and NC-8-F. NC-8 and NC-8-F exhibit more brittle properties than NC-5 and NC-5-F. Thus, their ultimate displacements are less than those of NC-5 and NC-5-F.

The NC-0 and NC-0-F load-displacement curves in Figure 15 show that the absence of transverse reinforcement results in the lowest shear load resistance, leading to the lowest maximum load and displacement compared to the NC-5, NC-5-F, NC-8, and NC-8-F counterparts. At a specific loading condition, the displacement in NC-0 is the most significant value compared to NC-5 and NC-8 due to the absence of transverse reinforcement. This behavior is also influenced by the quality of longitudinal reinforcement steel in NC-0, which is lower than that in NC-5 and NC-8, as described in Table 1. The ultimate load and displacement values in specimens NC-0 and NC-5, as well as in models of NC-0-F, NC-5-F, and NC-8-F, are shown in Table 2. The ultimate vertical loads in the NC-0-F, NC-5-F, and NC-8-F models are the same as those applied to the NC-0 and NC-5 specimens, with increments of 40 kN. The differences in the ultimate displacement values of the NC-0 and NC-5 specimens and the NC-0-F and NC-5-F numerical models are 7.909% and 1.563%, respectively. Thus, these models fulfil the accuracy criterion, with differences less than 10% [47,48]. The NC-8-F model was created to analyze the performance of flat slabs with an increased transverse reinforcement of 5ϕ8-72. This model represented a flat slab with denser transverse reinforcement in resisting punching shear. This condition results in a higher ultimate load of 616 kN but decreases ductility [56], as evidenced by the lower ultimate displacement of 19.178 mm compared with the NC-5 and NC-5-F counterparts. Table 3 shows crack loads and displacements, as well as the initial stiffnesses of NC specimens and models. The discrepancies are less than 10% which shows modeling accuracy [47,48].

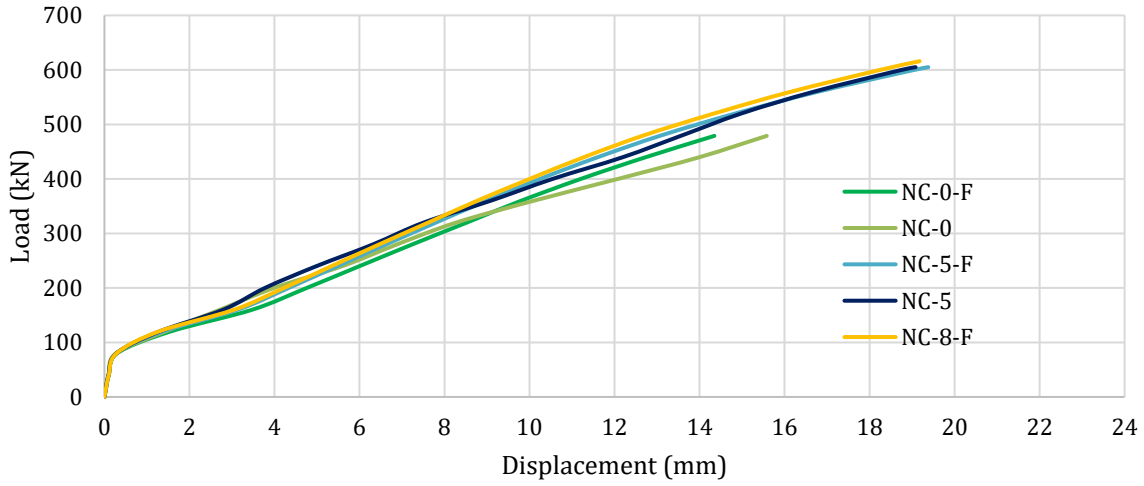

Fig. 15. Curves of load and displacement of the NC specimens and models

Table 2. Ultimate loads and displacements of NC specimens and models

Specimen			Model			
Type of flat slab	Ultimate load, F_u	Ultimate displacement, δ_u	Type of flat slab	Ultimate load, F_u	Ultimate displacement, δ_u	Difference
	(kN)	(mm)		(kN)	(mm)	(%)
NC-0	479	15.58	NC-0-F	479	14.35	7.91
NC-5	605	19.08	NC-5-F	605	19.38	1.56
-	-	-	NC-8-F	616	19.18	-

Table 3. Crack loads, displacements, and initial stiffnesses of NC specimens and models

Specimen				Model				
Type of flat slab	Crack load, F_{cr}	Crack displ., δ_{cr}	Initial stiffness, K_i	Type of flat slab	Crack load, F_{cr}	Crack displ., δ_{cr}	Initial stiffness, K_i	Discrepancy
	(kN)	(mm)	(kN/m)		(kN)	(mm)	(kN/m)	(%)
NC-0	80	0.269	0.297	NC-0-F	80	0.294	0.272	8.57
NC-5	80	0.282	0.283	NC-5-F	80	0.288	0.277	2.10
-	-	-	-	NC-8-F	80	0.285	0.280	-

3.1. Load-displacement Curves of GC Flat Slabs

The flat slab models with GC properties were incrementally vertically loaded by 40 kN until failure. The detailed dimensions, longitudinal and transverse reinforcement of the geopolymer flat slab models were the same as those of the NC flat slab specimens as described in Table 1. The GC-0-F flat slab model only achieved an ultimate load of 679 kN, while the GC-5-F and GC-8-F flat slab models achieved an ultimate load of 805 kN and 696 kN, respectively, as shown in Figure 16. The performance of GC-0-F in resisting shear loads was affected by the absence of transverse reinforcement in the slab. GC-5-F could withstand the highest shear load compared to the other two models. The GC-8-F model achieved lower ultimate shear load and displacement than the GC-5-F model because the larger transverse reinforcement diameter imparted brittle behavior [56], leading the flat slab to collapse more rapidly.

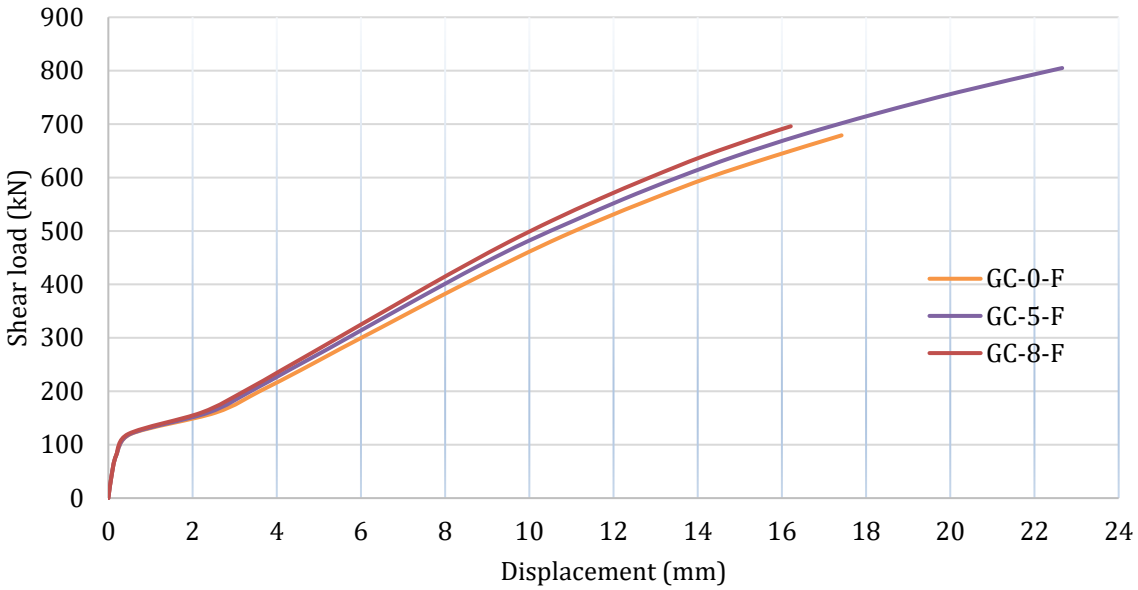

Fig. 16. Curves of load and displacement of GC-0, GC-5, and GC-8 models

Table 4 shows the crack, ultimate shear load, and displacement of GC flat slab models with different shear reinforcement configurations. All GC models cracked at a load of 120 kN, which was higher than the crack load of the NC specimens and models. The crack deflection in the GC models was greater than that experienced by the NC specimens and models. This indicates that the GC flat slab performed better under elastic conditions before cracking. Initial stiffness increases with the diameter of the transverse reinforcement. The ultimate shear load of each GC flat slab model is higher than that of an NC flat slab with the same reinforcement details. The GC-0-F, GC-5-F, and GC-8-F flat slab models achieved ultimate shear loads of 679 kN, 805 kN, and 696 kN, respectively. The $\phi 8$ reinforcement tends to produce a stiffer but less ductile response in the GC-8-F flat slab, leading to a lower ultimate shear load than in the GC-5-F flat slab. The GC-5-F model achieved the highest

ultimate shear force and displacement among the flat slab models, surpassing the GC-0-F and GC-8-F models.

The GC-0-F flat slab model without transverse reinforcement failed to resist the ultimate shear load. This behavior differs from the NC-0-F flat slab model owing to the higher compressive strength of GC compared to NC, leading to a higher ultimate load. However, the absence of transverse reinforcement reduced the shear capacity. Thus, the GC material could not resist the ultimate shear load. In the GC-0-F flat slab model, concrete crushing occurred, followed by failure at the ultimate condition [17]. The ultimate shear achieved by the GC-0-F flat slab model was 679 kN, with a difference of 200 kN compared to the NC-0-F counterpart, which only achieved an ultimate shear of 479 kN. It indicated that the higher compressive strength of GC needs to be supported by transverse reinforcement in resisting shear loads.

Table 4. Crack, ultimate load, and displacement of GC models

Type of flat slab	Model				
	Crack load, F_{cr}	Crack displacement, δ_{cr}	Initial stiffness, K_i	Ultimate load, F_u	Ultimate displacement, δ_u
	(kN)	(mm)	(kN/mm)	(kN)	(mm)
GC-0-F	120	0.530	0.227	679	17.418
GC-5-F	120	0.518	0.232	805	22.658
GC-8-F	120	0.471	0.255	696	16.211

The microstructure of GC also influences the difference in behavior of NC and GC flat slabs. The fly ash-based, low-calcium binder content in GC affects shear and bond behavior differently than in NC. Geopolymer concrete in a previous study [57] contained low-calcium fly ash, fine and coarse aggregates, and an alkaline solution. The test specimens, consisting of geopolymer blocks, were subjected to a concentrated downward vertical load. The average first cracking load and ultimate deflection of the geopolymer blocks were 22% higher than those of conventional concrete. It indicates that the inter-matrix bond in the geopolymer concrete mixture has greater adhesive strength than conventional concrete. Fly ash-based geopolymer concrete produces lightweight fine aggregate with a stronger bond than fly ash-based geopolymer concrete using quartz aggregate [58]. It is consistent with research on the relationship between density and concrete compressive strength. The lighter the concrete density, the stronger the bond [59].

The shear strength of both conventional and geopolymer concrete is significantly influenced by the concrete's compressive strength [60]. Shear cracking and the ultimate shear capacity of geopolymer blocks increase with increasing concrete strength [61]. Factors that influence the strength of the matrix bond in resisting shear are the type and content of fly ash, concrete compressive strength, sodium hydroxide (NaOH) concentration [62-69] with an optimum concentration of around 12% to 14% and molarity (solution concentration expressed in moles per liter of solution) of 10M to 15M, aggregate to binder mass ratio, mix design, curing, and coating [68].

3.2. Stress Contour of NC Flat Slabs

Stress contours are used to visualize the stress distribution on a flat slab in several colors within a specific stress range. Stress contours provide information on the location of structural elements susceptible to failure or damage based on the stress they cause, as well as the locations of maximum and minimum stresses. Compressive and tensile stresses are expressed as negative and positive values, respectively. When a flat slab is subjected to a monotonic load, the structure responds by resisting compressive or tensile stresses depending on the placement and loading location. Figure 17 (a) shows the top of the NC-0-F flat slab, including the areas around the columns and four spreader beams. The orange compressive stresses of 3-12 MPa indicate that the NC-0-F flat slab experiences compressive stresses lower than the normal concrete compressive strength of 30 MPa. Some parts of the two spreader beams and a few small yellow areas experience compressive stresses of 12-21 MPa. The red areas on the top of the columns, slab, and spreader beams

experienced stresses from 3 MPa compression to 6 MPa tension. Although the dominant stress in the red areas is compressive, the stress contours extend to 6 MPa of tensile stress. Figure 17 (b) shows the area around the columns for the NC-5-F flat slab with compressive stresses of 3-12 MPa (orange) and 12-21 MPa (yellow), which are wider than those for the NC-0-F flat slab. This is due to the NC-5-F flat slab experiencing higher shear loads and ultimate displacements than NC-0-F, resulting in higher compressive stress. The stress contour of the NC-8-F flat slab is shown in Figure 17 (c). The area around the column is fitted with shear reinforcement, resulting in an ultimate shear load that produces compressive stresses of 3-12 MPa (orange) and 12-21 MPa (yellow). The stress area in NC-8-F is similar to that of NC-5-F. It indicates that increasing the reinforcement diameter from 5 mm to 8 mm does not increase the ultimate stress.

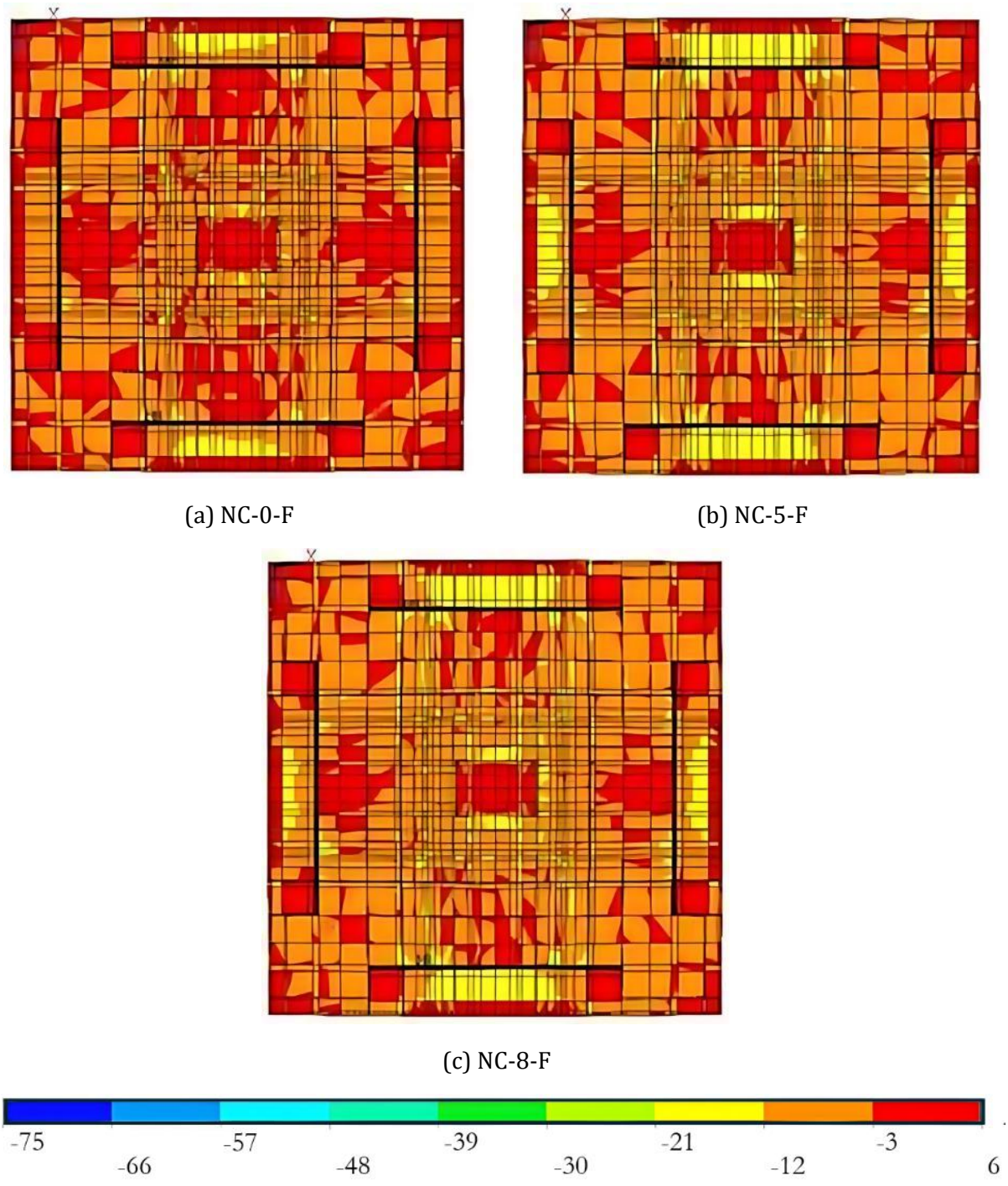

(a) NC-0-F (b) NC-5-F

(c) NC-8-F

Fig. 17. Top side of stress contours of the NC flat slab models

The crack patterns in NC-0 and NC-5 specimens are shown in Figure 18. Due to the loading on the top of the column and four spreader beams placed on the flat slab, punching shear failure occurred in NC-0 and NC-5 [41]. The crack pattern that occurred in the NC-0 specimen in Figure 18(a) corresponds to the stress contour of NC-0-F in Figure 17(a). The four spreader beams and the flat slab experienced compressive stresses of 3 to 21 MPa, which led to punching shear. Specimen NC-5 experienced punching shear failure, with the area around the column formed by cracks in the flat slab in Figure 18(b) being broader than that of NC-0. This correlates to the stress contour of NC-5-F in Figure 17(b), where the compressive stress area of 12 to 21 MPa is wider than that of NC-0-F.

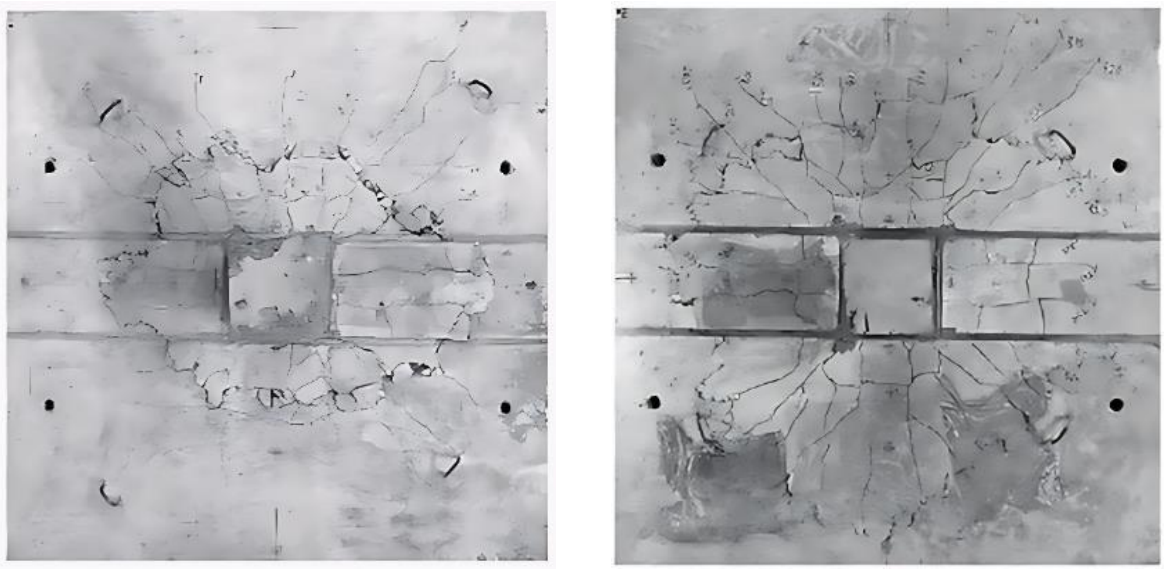

(a) Crack pattern of the NC-0 specimen (b) Crack pattern of the NC-5 specimen

Fig. 18. Top side of the crack pattern of the NC flat slab specimens [41]

Figure 19(a) shows the red stress contour on the bottom side of the NC-0-F flat slab, which is predominantly subjected to tensile stress just below the column. The slab area around the column is indicated in light and dark green, with maximum compressive stresses of 21-30 MPa and 30-39 MPa, respectively. It shows that the dark green area fails due to compressive stress exceeding the normal concrete compressive strength of 30 MPa. This behavior indicates that the bottom side of the slab is more prone to failure than the top side, owing to the top side being compressed and resisted by the concrete, while the bottom side withstands tensile loads through longitudinal reinforcement [70].

Figure 19(b) shows the stress that occurs around the column on the NC-5-F flat slab with a larger area due to monotonic loads on the top side of the column and the spreader beam support indicated by light green, dark green, turquoise, and light blue with compressive stresses of 21-30 MPa, 30-39 MPa, 39-48 MPa, and 48-57 MPa, respectively. It shows that the area experiencing collapse is wider because the presence of $5\phi5$ shear reinforcement of NC-5-F flat slab causes the ultimate shear load to be higher than that of the NC-0-F flat slab. Most of the compressive stress in the flat slab does not exceed the concrete compressive strength of 30 MPa, which is indicated by light green (21-30 MPa), yellow (12-21 MPa), and orange (3-12 MPa).

Figure 19(c) shows the stress that occurs in the area around the column in the NC-8-F flat slab with light green, dark green, a little turquoise green, and a little light blue with maximum stress of 21-30 MPa, 30-39 MPa, 39-48 MPa, and 48-57 MPa, respectively. Most of the stress contours in yellow (12-21 MPa) and orange (3-12 MPa) do not exceed the concrete compressive strength of 30 MPa. The area of the 12-21 MPa compressive stress contour (yellow) is wider on the NC-8 flat slab than on the NC-5 flat slab because the achieved ultimate shear load is higher.

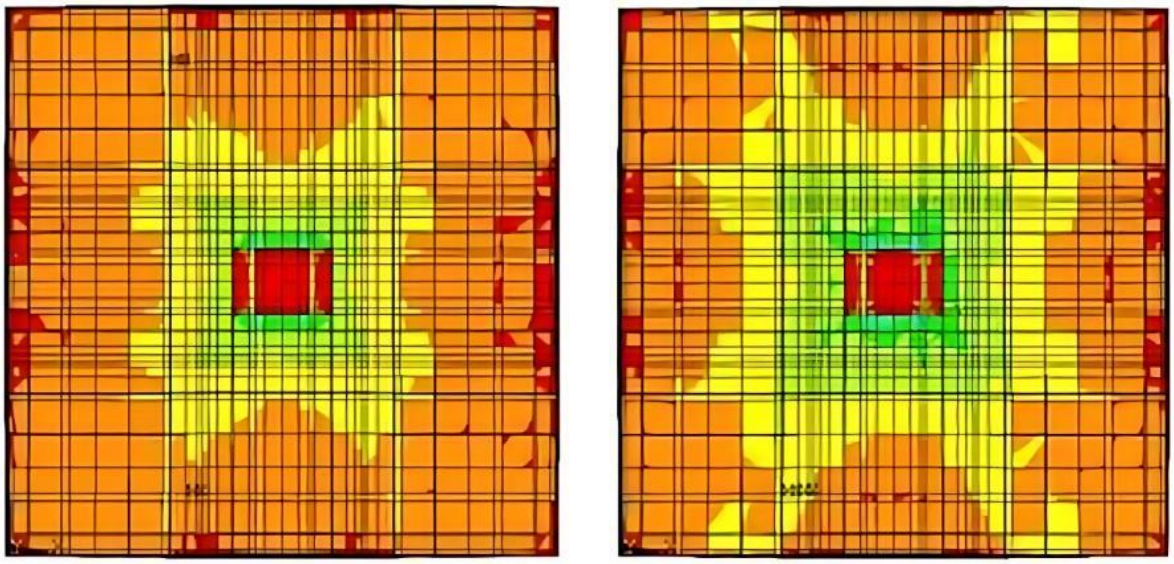

(a) NC-0-F (b) NC-5-F

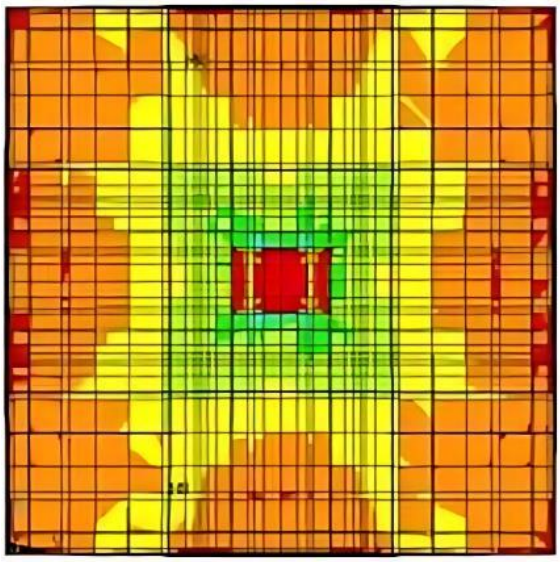

(c) NC-8-F

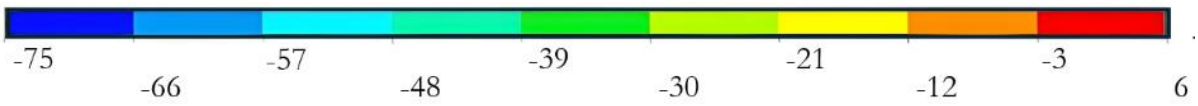

Fig. 19. Bottom side of stress contours of the NC flat slab models

3.3. Stress Contour of GC Flat Slab Models

Figure 20(a) shows the stress contours of the top side of the flat slab around the column and the spreader beam supports for the GC-0-F flat slab without shear reinforcement in the slab around the column. Compressive stresses of 1.08-9.13 MPa (orange), 9.16-17.23 MPa (yellow) are distributed and dominate the slab. The slab parts around the column experience a greater compressive stress of 17.23-25.31 MPa (light green). There is a small area that experiences a compressive stress exceeding the concrete compressive strength (30 MPa), namely 25.31-33.39 MPa (dark green). The middle of the four spreader beams experiences greater compressive stress than the ends, at 9.16-17.23 MPa (yellow) and 17.23-25.31 MPa (light green). Each end of the spreader beam and column experiences a lower compressive stress of 1.08 MPa (compression) to 7 MPa (tensile). Although the red stress contour is predominantly compressive, the color display includes tensile stress.

Figure 20(b) shows the top side of the GC-5-F flat slab. The compressive stress of 9.16-17.23 MPa (yellow) in the slab occurs over a larger area than the GC-0-F flat slab. A higher compressive stress of 25.31-33.39 MPa (dark green) develops in the middle of the two spreader beams. It occurs because the ultimate shear load in GC-5-F is higher than that of the GC-0-F flat slab due to the presence of 5ϕ5 shear reinforcement around the columns. The stress distribution on the top side of the GC-8-F flat slab in Figure 20(c) shows that the ultimate shear load is almost the same as that of GC-0-F, causing similar stress behavior. The use of 5ϕ8 shear reinforcement around the columns causes the flat slab to become brittle and reduces the shear load and ultimate displacement [55]. The GC-8-F model experiences lower compressive stress at the ultimate condition than the GF-5-F model due to its less ductile behavior (Table 7). Since the ultimate load of the GC-8-F model is lower than that of the GC-5-F (Tables 2 and 4), its ultimate compressive stress is lower. The GC-5-F model achieves a compressive stress of 25.31 to 33.39 MPa (dark green), while the GC-8-F model only achieves a compressive stress of 17.23 to 25.31 MPa (light green) on the top side of the flat slab as shown in Figures 20(b) and (c).

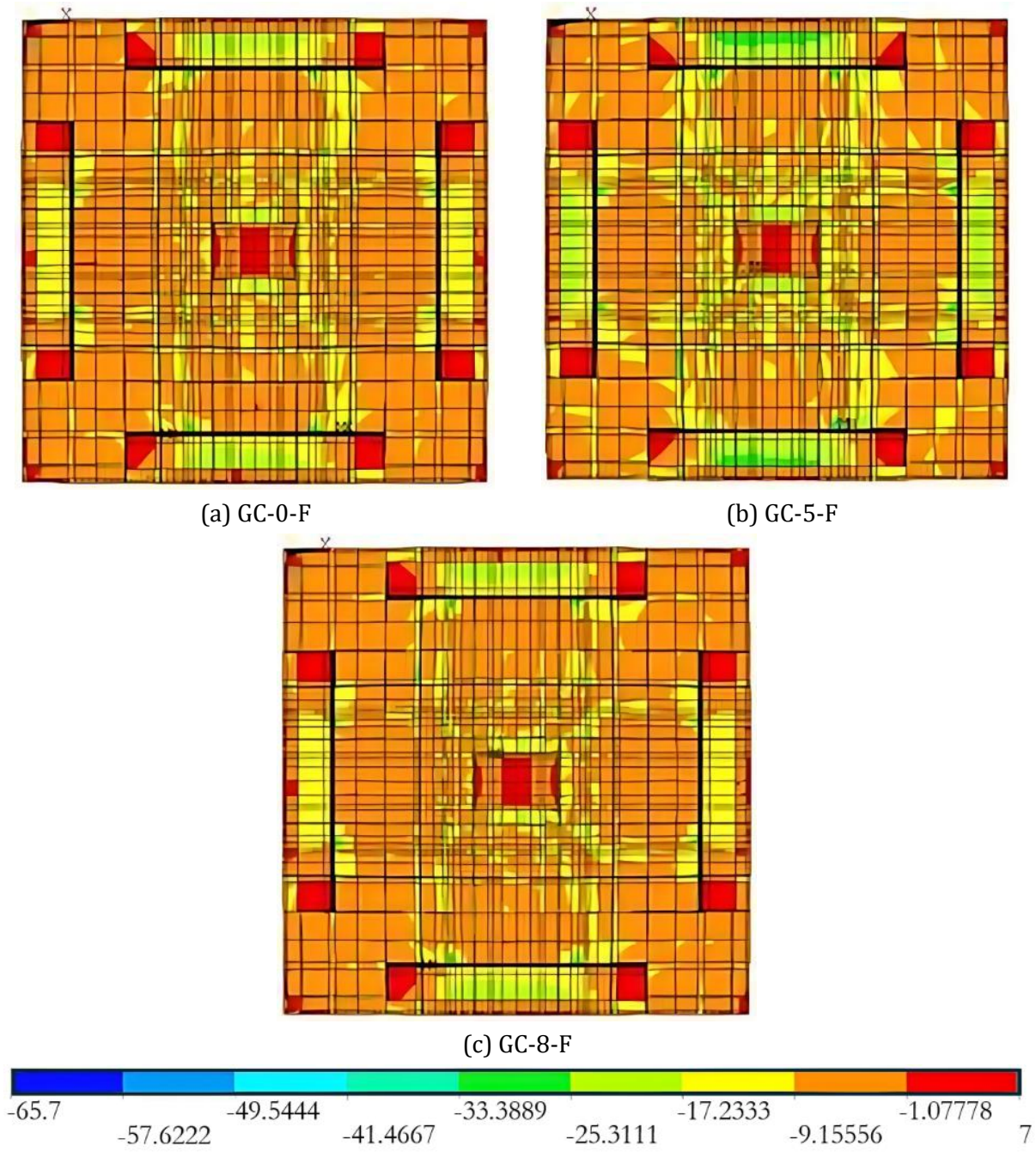

(a) GC-0-F (b) GC-5-F

(c) GC-8-F

Fig. 20. Top side of stress contours of the GC flat slab models

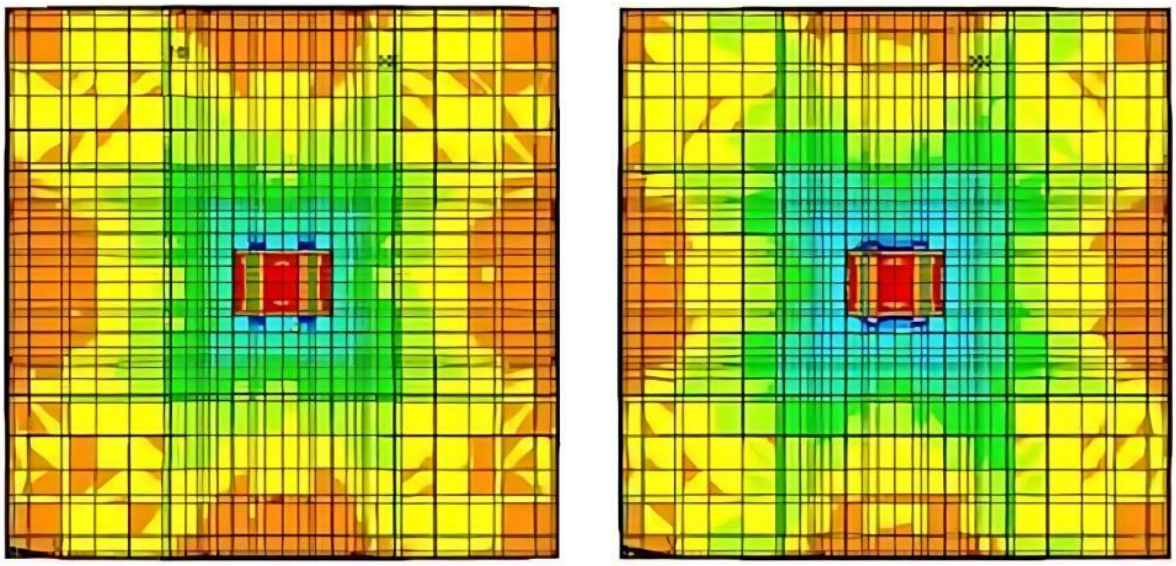

(a) GC-0-F (b) GC-5-F

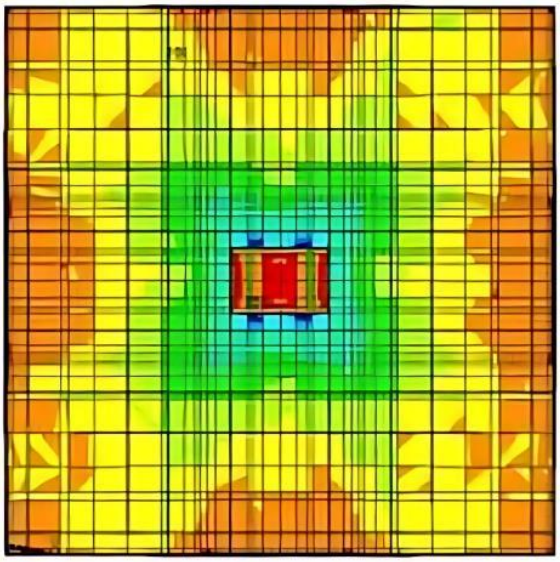

(c) GC-8-F

Fig. 21. Bottom side of stress contours of the GC flat slab models

Figure 21(a) depicts the compressive stress on the underside of the GC-0-F flat slab that occurs in the area around the column. There are small areas colored turquoise, light blue, and blue with compressive stress ranges of 33.39-41.47 MPa, 41.47-49.54 MPa, and 49.54-57.62 MPa, respectively. An area of the highest compressive stress contour of 57.62-65.7 MPa appears on the slab directly below the column perimeter. This indicates that this area is experiencing significant collapse due to flat slab compressive stress exceeding the GC compressive strength of 41.5 MPa. However, most flat slabs survive failure and experience compressive stress below 41.5 MPa, as shown by the red-to-turquoise-green areas with the highest compressive stress of 41.5 MPa. The underside of the column exhibits the smallest compressive stress in red (1.08 MPa to 7 MPa-tensile stress) and orange (1.08 to 9.16 MPa).

Figure 21(b) depicts the compressive stresses that occur in the area around the wider column indicated by light blue, blue, and dark blue with values of 41.47-49.54 MPa, 49.54-57.62 MPa, and 57.62-65.70 MPa, respectively, which exceed the compressive strength of geopolymer concrete of 41.5 MPa. It indicates a wider collapse occurred owing to the achievement of a higher ultimate

shear load than that achieved in the GC-0-F flat slab in this area. The presence of 5ϕ5 shear reinforcement increases the shear capacity of the slab [55]. The GC-8-F flat slab shows a very similar stress contour distribution to its GC-0-F counterparts because these flat slabs achieve very close values of ultimate shear loads, as shown in Figure 21(c). The use of 8 mm diameter shear reinforcement in the GC-8-F flat slab results in less ductile behavior that restricts it from developing deformation that leads to a lower ultimate shear load than the GC-5-F flat slab. This condition also influences the stress. The bottom side of the flat slab of the GC-8-F model at the ultimate condition reaches a compressive stress of 41.47 – 49.54 MPa (light blue) and 57.62 – 65.7 MPa (dark blue) in a narrower area than that of the GC-5-F model, as shown in Figures 21 (b) and (c). It is because the ultimate load on the GC-8-F model is lower than that of the GC-5-F model. This compressive stress exceeded GC compressive strength of 41.5 MPa in the light and dark blue areas and lead to the ultimate condition.

3.4. Displacement Contours of the NC Flat Slab Models

Displacement contours show the positions of the elements and nodes of the flat slabs under vertical downward monotonic loads. The achieved ultimate loads vary across flat slab models owing to the shear capacity provided by the longitudinal and transverse reinforcements. This condition affects the magnitude of the displacement expressed in the contours. The ultimate load of the NC-0-F flat slab is 479 kN with an ultimate displacement of 15.581 mm. Figure 22(a) shows the dominant downward vertical displacement on the four edges of the flat slab due to the application of monotonic loads on the four spreader beams of 14.61 to 17.58 mm (turquoise green). The displacement of the flat slab towards the center decreases because the load pressure from the spreader beam is reduced. It can be seen with displacements of 8.67 to 11.64 mm (yellow), 2.72 to 5.69 mm (orange), and +0.25 to 2.72 mm (red). The columns and the center of the flat slab experience the same range of displacements. Figure 22(b) shows the displacement contour of the NC-5-F flat slab. The presence of ϕ5-72 transverse reinforcement increases the ultimate load and displacement, resulting in larger displacements than the NC-0-F counterpart, which are 23.53-26.50 mm (dark blue) at the four corners of the flat slab, 20.56-23.53 mm (medium blue) at the four edges, and 17.58-20.56 mm (light blue) at the spreader beams. The magnitude of the displacement decreases as the element location approaches the center, resembling that of the NC-0-F flat slab. The NC-8-F flat slab has ϕ 8-72 transverse reinforcement. Thus, it achieves the highest ultimate load among all other models but exhibits a lower ultimate displacement than the NC-5-F flat slab, with a difference of 1.06% (Table 2), as shown in Figure 22(c). In general, the displacement in the NC-8-F flat slab is similar to that of NC-5-F. It shows that increasing the percentage of transverse reinforcement does not result in a significant difference in the displacement contour. Otherwise, the addition of transverse reinforcement reduces ductility and leads to a lower ultimate displacement.

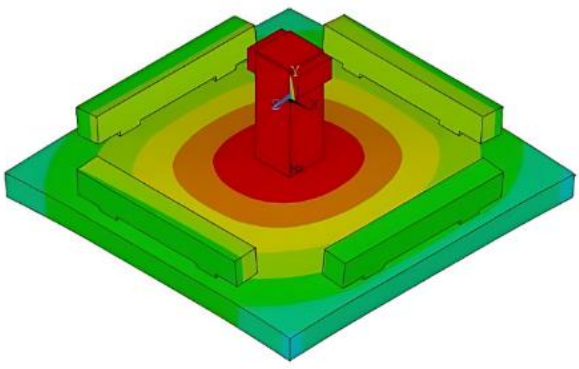

(a) NC-0-F under load of 479 kN

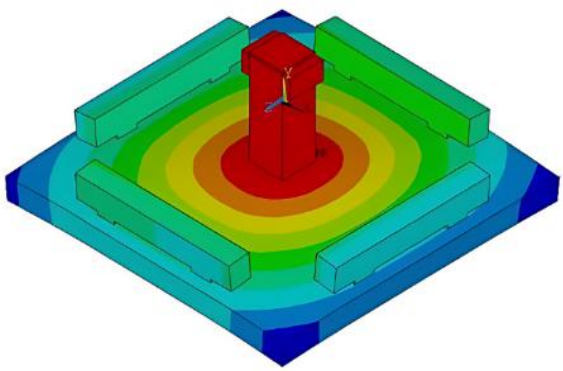

(b) NC-5-F under load of 605 kN

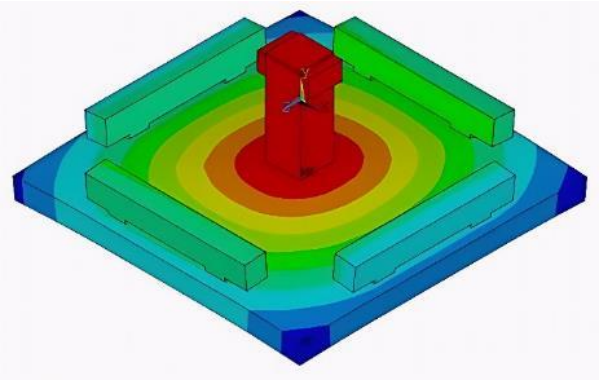

(c) NC-8-F under load of 616 kN

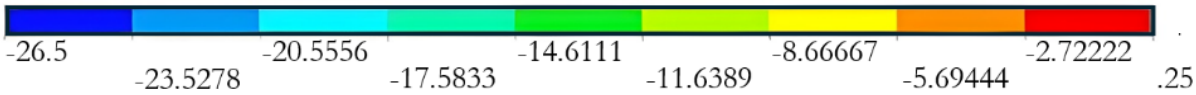

Fig. 22. Top side of displacement contours of the NC flat slab models

3.5. Displacement Contours of the GC Flat Slab Models

The downward displacement contour of GC-0-F in Figure 23(a) shows the position of the four corners of the flat slab that experienced the most significant displacement compared to other parts, namely 20.92-24.44 mm (light blue). The four edges of the flat slab performed smaller displacements, ranging from 17.39 to 20.92 mm (turquoise green). Spreader beams that received monotonic loads exhibited displacements of 13.86-17.39 MPa (dark green). The displacements decreased towards the center of the flat slab, ranging from 10.33 to 13.86 mm (light green), 6.80 to 10.33 mm (yellow), 3.28 to 6.81 mm (orange), and +0.25 (upward) to 3.28 mm (red). The displacements in the GC-0-F flat slab were greater than those of the NC-0-F counterpart owing to the presence of GC material that provided a greater capacity to withstand monotonic loads at the ultimate condition. The GC-5-F flat slab in Figure 23(b) achieved a greater ultimate displacement than the GC-0-F flat slab owing to the shear load capacity from the ϕ5-72 transverse steel bars. The four corners of the GC-5-F flat slab sustained displacements of 27.97-31.50 mm (dark blue). On the side towards the center at the corners of the flat slab, the displacements reached 24.44-27.97 mm (medium blue). Towards the center of the flat slab, the displacements decreased to 20.92-24.44 mm (light blue), 17.39-20.92 mm (turquoise green) on the spreader beams, 13.86-17.39 mm (dark green), 10.33-13.86 mm (light green), 6.81-10.33 mm (yellow), 3.28-6.81 mm (orange), and +0.25-3.28 mm (red).

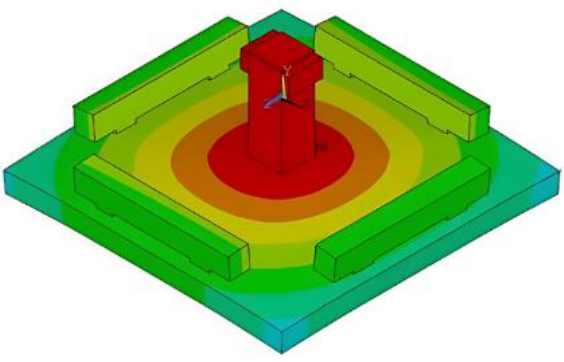

(a) GC-0-F under load of 679 kN

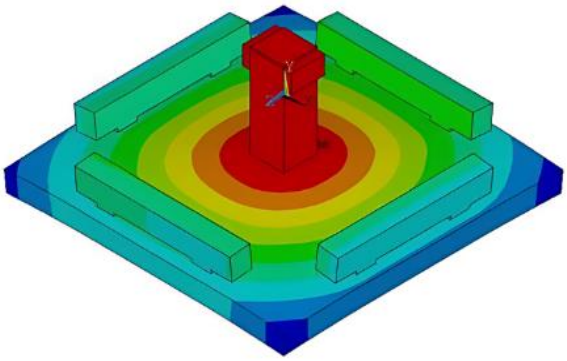

(b) GC-5-F under load of 805 kN

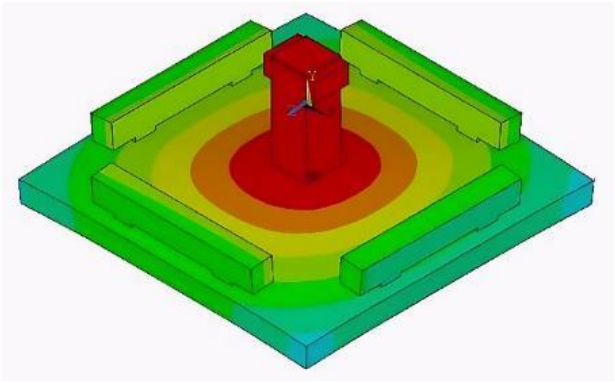

(c) GC-8-F under load of 696 kN

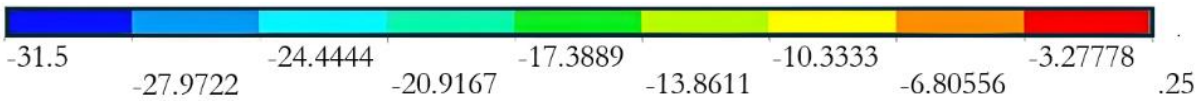

Fig. 22. Top side of the displacement contours of the GC flat slab

Figure 23(c) shows the contours of the displacements of the GC-8-F flat slab. The presence of transverse reinforcement with a larger diameter in the GC-8-F flat slab, compared with that in the GC-5-F counterpart, resulted in brittle behavior [55]. The ultimate displacement in GC-8-F was only 16.211 mm (Table 3), with a maximum displacement range of 20.92-24.44 mm (light blue) at the four corners. The four edges of the GC-8-F flat slab and spreader beams performed displacements of 17.39-20.92 mm (turquoise green). The displacements decreased toward the center and resembled those in the GC-0-F counterpart.

3.6. Ductility of NC Flat Slab Specimens

Ductility is the ratio of the ultimate displacement (Δu) to the yield displacement (Δy) [71]. Ductility represents the ability of a structure to deform and withstand loads up to the ultimate condition before failure [56,72]. The position of the yield point on the load-displacement relationship curve was determined by the method of equality of areas above and below the curve formed by the two linear lines [73]. The determination of the yield point from the load-displacement curve of the NC-0 flat slab specimen is shown in Figure 24. Table 5 shows the yield load (F_y), yield displacement (δ_y), ultimate load (F_u), ultimate displacement (δ_u), and ductility ratio. Using the same method, the yield point position of the NC-5 specimen was obtained. The ductility ratio of the NC-0 and NC-8 flat slab specimens is less than 2.0, and thus they are categorized as low-ductility [73]. The brittle nature of these specimens was due to the slab's large area, which provided adequate stiffness and resisted monotonic loads. The NC-5 flat slab specimen exhibited higher ultimate loads and displacements due to the presence of ϕ5-72 transverse reinforcement, which increased the shear capacity.

Table 5. Yield load, yield displacement, and ductility of NC specimens

Type of flat slab (experimental)	Yield		Ultimate		Ductility ratio
	Load, F_y	Displacement, δ_y	Load, F_u	Displacement, δ_u	
	(kN)	(mm)	(kN)	(mm)	μ
NC-0	451.433	11.271	479	15.580	1.382
NC-5	557.335	13.895	605	19.380	1.395

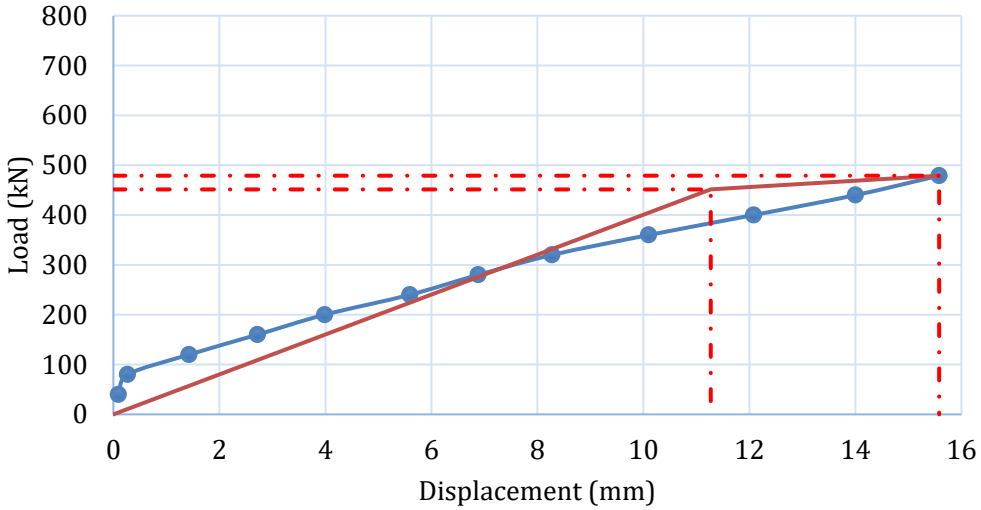

Fig. 24. Yield point determination of NC-0 specimen

3.7. Ductility of NC Flat Slab Models

Using the similarity area method [73], the yield loads and displacements were obtained for the flat slab models of NC-0-F, NC-5-F, and NC-8-F. The presence of ϕ5-72 transverse reinforcement increased the shear capacity, thus slowing the yield condition in the NC-5-F than the NC-0-F flat slab. Similarly, the ϕ8-72 transverse reinforcement in the NC-8-F model delayed the yield condition compared to NC-5-F. However, the larger shear reinforcement area led to more brittle behavior. Thus, the ultimate displacement of the NC-8-F flat slab was lower than that of NC-5-F even though its ultimate load was higher. This reinforcement resulted in a lower ductility ratio in the NC-8-F compared to the NC-5-F flat slab. All NC flat slab models exhibited ductility ratios of less than 2, as shown in Table 6; thus, they were categorized as low ductile. It was owing to the large area of the flat slab, which provided a high stiffness, resulting in low ultimate displacements. The differences in the ductility ratios of the NC-0 specimen and NC-0-F model are 9.70%, while the NC-5 specimens and NC-5-F model exhibit a 1.08% discrepancy in the ductility ratio.

Table 6. Determination of the yield point and ductility ratios of NC flat slab models

Type of flat slab (model)	Yield		Ultimate		Ductility ratio
	Load	Displacement	Load	Displacement	
	F_y (kN)	δ_y	F_u (kN)	δ_u	μ
NC-0-F	458.416	11.498	479	14.349	1.248
NC-5-F	562.040	14.041	605	19.381	1.380
NC-8-F	603.130	14.951	616	19.178	1.283

3.8. Ductility of GC Flat Slab Models

The ductility ratios of the GC flat slab models are shown in Table 7. Each GC flat slab ductility ratio is higher than its NC counterpart. This behavior indicates that the GC material influences flat slab properties by increasing ductility. However, all GC flat slab models are categorized as low-ductility due to ratios below 2 [73,74]. The GC-5-F flat slab model is more ductile than the GC-0-F counterpart, owing to higher ultimate loads and displacements supported by the presence of ϕ5-72 transverse reinforcement that provided a higher shear capacity. However, the excessive transverse reinforcement of ϕ8-72 resulted in a lower ductility ratio for the GC-8 flat slab than the GC-5 counterpart. This behavior is similar to NC-8-F, which exhibits less ductility compared to NC-5-F in Table 6. The transverse reinforcement of ϕ8-72 and the higher compressive strength of GC (41.5 MPa) compared to NC (30 MPa) decrease ductility. Thus, the GC-8-F model achieves a smaller ultimate displacement than GC-5-F, as shown in Table 7.

Table 6. Determination of the yield point and ductility ratios of NC flat slab models

Type of flat slab (model)	Yield		Ultimate		Ductility ratio
	Load	Displacement	Load	Displacement	
	F_y (kN)	δ_y	F_u (kN)	δ_u	μ
NC-0-F	458.416	11.498	479	14.349	1.248
NC-5-F	562.040	14.041	605	19.381	1.380
NC-8-F	603.130	14.951	616	19.178	1.283

Table 7. Determination of yield point and ductility ratios in GC flat slab models

Type of flat slab (model)	Yield		Ultimate		Ductility, μ	Differences with NC models
	Load, F_y	Displacement, δ_y	Load, F_y	Displacement, δ_y		
	(kN)	(mm)	(kN)	(mm)		(%)
GC-0-F	616.781	12.814	679	17.418	1.359	8.920
GC-5-F	760.042	16.301	805	22.658	1.390	0.696
GC-8-F	649.661	12.382	696	16.211	1.309	2.071

3.9. Stiffness of NC Flat Slab Specimens

Stiffness is the ratio of load to displacement at a specific loading condition. As the load increases monotonically, expressed in Time Load, the stiffness of a flat slab decreases due to extended element damage. Stiffness degradation occurs due to the reduced capacity and is expressed as the ratio of the stiffness to the yield stiffness. The curves that correlate stiffness and stiffness degradation with Time Load on NC-0 and NC-5 specimens are shown in Figures 25 and 26, respectively. The stiffness of NC-0 and NC-5 flat slabs at the 1st load step was 419.697 kN/mm and 424.513 kN/mm, respectively. At the 2nd and 3rd load steps, the stiffness dropped drastically to 297.319 kN/mm and 83.996 kN/mm for NC-0, while at NC-5, the stiffnesses were 283.297 kN/mm and 93.042 kN/mm. Since the 4th load step, the stiffness was relatively stable, although it continued to decrease through the 12th load step for NC-0 and the 16th for NC-5. At the 4th Time Load, the stiffness of NC-0 was 58.825 kN/mm. It continued to decrease to 30.742 kN/mm. The stiffness of the NC-5 flat slab at the 4th Time Load was 57.255 kN/mm. It revealed that the significant damage to the concrete occurred at the 2nd and 3rd load steps. Furthermore, concrete cracks and yielded steel bars occurred, but did not cause a drastic decrease in stiffness. It followed the load-displacement relationship curve of the NC-0 and NC-5 flat slab specimens in Figure 15.

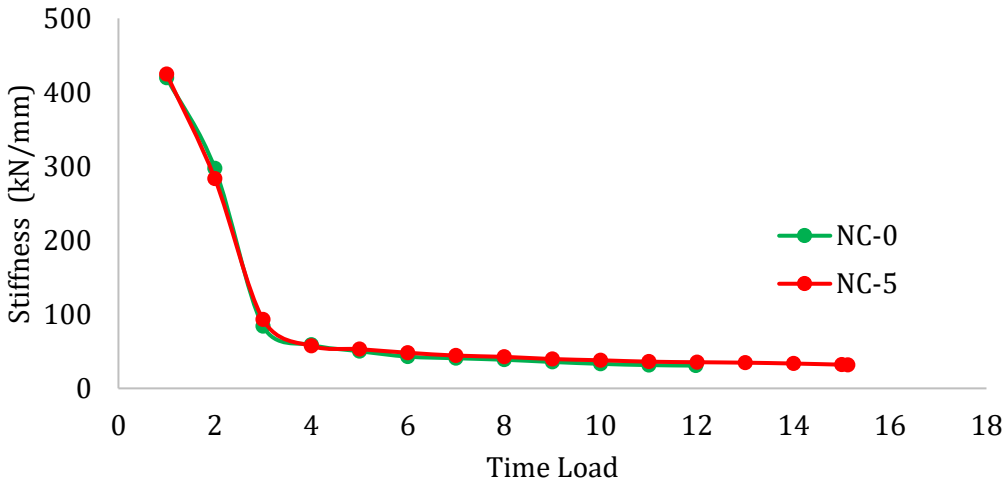

Fig. 25. Curves of stiffness of NC-0 and NC-5 specimens

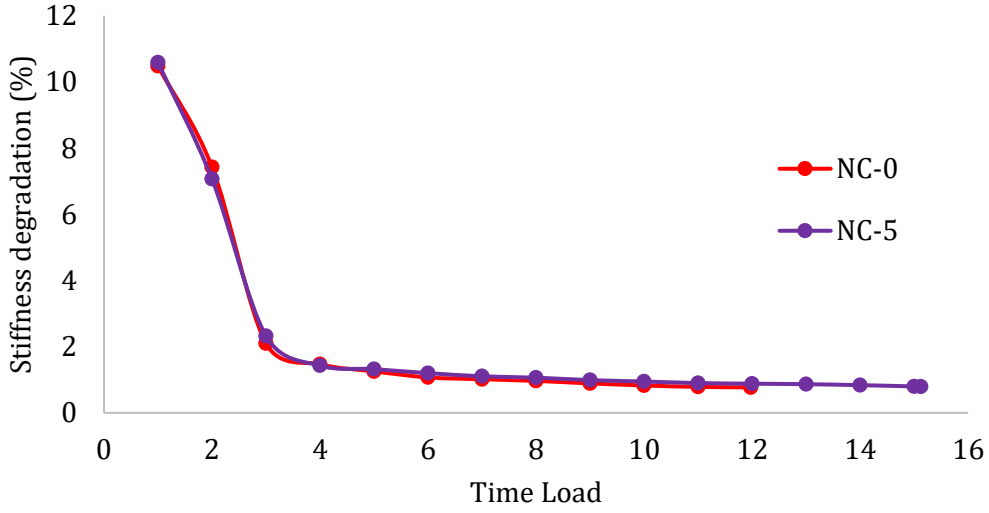

Fig. 26. Curves of stiffness degradation of NC-0 and NC-5 specimens

The behavior of the flat slab, as shown in the stiffness degradation curve, resembles the stiffness curve. Significant degradation occurred at Time Loads 1, 2, and 3, with 10.479%, 7.423%, and 2.097% in NC-0, and 10.584%, 7.063%, and 2.320% in NC-5. Furthermore, there was a gradual stiffness degradation in NC-0 from 1.469% to 0.768%. In NC-5, the stiffness degradation at Time Load 4 was 1.427% and continued to decrease slowly to 0.790%. The NC-5 flat slab exhibited greater stiffness and stiffness degradation than its NC-0 counterpart. This behavior was shown by the lower ultimate load of the NC-0 than that of the NC-5 flat slab.

3.10. Stiffness of NC Flat Slab Models

The stiffness relationship curve with Time Load of NC-0-F, NC-5-F, and NC-8-F flat slab models is shown in Figure 27. In general, the stiffness behavior of the NC-0-F flat slab model resembles the NC-0 specimen, and the NC-5-F model resembles the NC-5 specimen. The NC-0-F flat slab model has a drastically reduced stiffness of 396,660 kN/mm, 271,830 kN/mm, and 77,432 kN/mm at Time Loads 1, 2, and 3, respectively. The stiffness at Time Load 4 to 12 decreased more slowly from 46,059 kN/mm to 33,383 kN/mm. In the NC-5-F and NC-8-F flat slab models, the stiffness change behavior was relatively the same: at Time Loads 1 to 4, there was a drastic decrease, then slowed until the ultimate condition at Time Load 16. In the NC-5-F flat slab, Time Load 1, 2, 3, 4, and 16, the stiffnesses were 396.888 kN/mm, 277.345 kN/mm, 87.537 kN/mm, 51.074 kN/mm, and 31.216 kN/mm, respectively. The NC-8-F flat slab model performed stiffnesses of 397.164 kN/mm, 280.261 kN/mm, 94.286 kN/mm, 52.469 kN/mm, and 32.120 kN/mm at the same Time Loads.

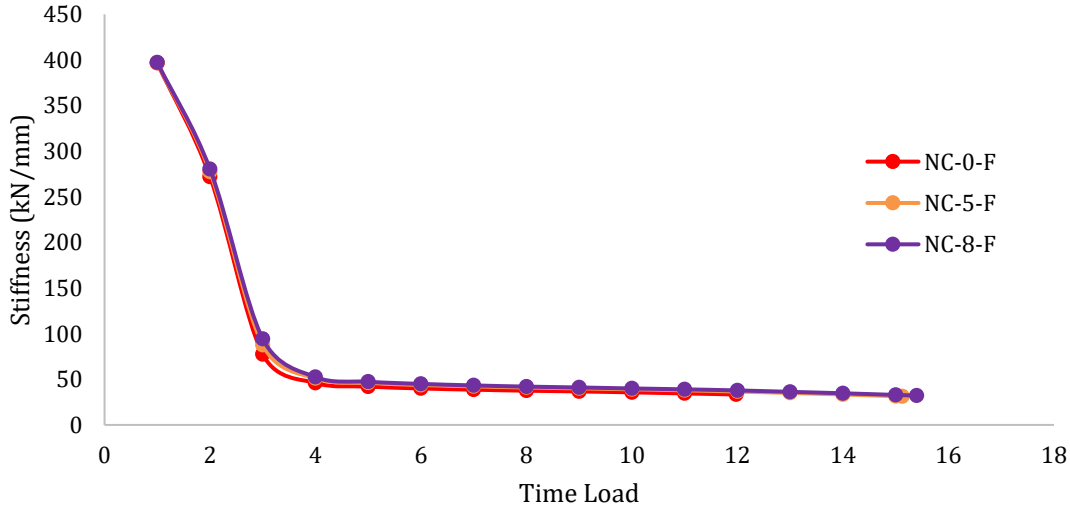

Fig. 27. Curves of stiffness of NC-0-F, NC-5-F, and NC-8-F models

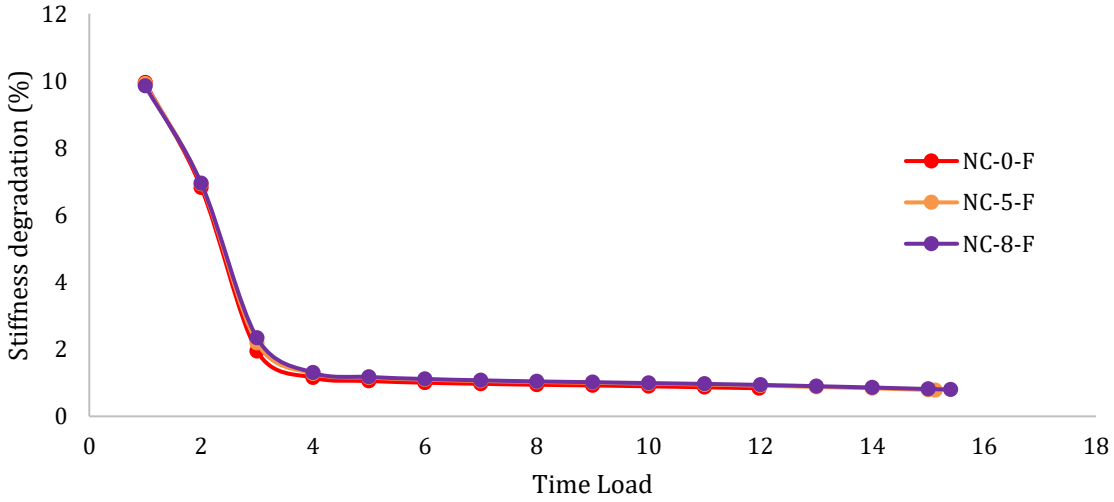

Fig. 28. Curves of stiffness degradation of NC-0-F, NC-5-F, and NC-8-F models

Overall, the stiffness of the NC-8-F flat slab was higher than that of its NC-5-F and NC-0-F counterparts. This was due to higher loads on the NC-8-F flat slab model compared to the NC-5-F and NC-0-F flat slab models, as shown in the transverse reinforcement areas. Figure 28 depicts the percentage of stiffness degradation that occurred drastically at Time Load 1 to 4 in the NC-0-F, NC-5-F, and NC-8-F models. Then, stiffness degradation slowed down at Time Load 5 until the ultimate condition at the end of loading. Stiffness degradations at Time Load 1, 2, 3, 4, and 12 in NC-0-F were 9.949%, 6.818%, 1.942%, 1.155%, and 0.837%. Stiffness degradations of NC-5-F at Time Load 1, 2, 3, 4, and 16 were 9.915%, 6.929%, 2.187%, 1.276%, and 0.780%. At the same Time Load, the degradations of the NC-8-F flat slab model were 9.846%, 6.948%, 2.337%, 1.301%, and 0.796%. The comparisons of initial stiffness, crack load, and ultimate displacement between the specimens and NC models are shown in Table 8. The difference between the NC specimens and models is less than 10%. Thus, the NC models are categorized as accurate [47,48].

Table 8. Stiffness of NC specimens and models

Specimen				Model				
Type of flat slab	Crack load, F_{cr}	Crack displ., δ_{cr}	Initial stiffness, K_i	Type of flat slab	Crack load, F_{cr}	Crack displ., δ_{cr}	Initial stiffness, K_i	Difference
	(kN)	(mm)	(kN/m)		(kN)	(mm)	(kN/mm)	(%)
NC-0	80	0.269	0.297	NC-0-F	80	0.294	0.272	8.57
NC-5	80	0.282	0.283	NC-5-F	80	0.288	0.277	2.10
-	-	-		NC-8-F	80	0.285	0.280	

3.11. Stiffness of GC Flat Slab Models

The stiffness behavior of a flat slab made of GC material was almost similar to that of its counterpart using NC material. Stiffness decreased rapidly from Time Load 1 to 4, then slowly reduced from Time Load 5 until the end of loading at the ultimate condition. The difference was that the Time Load on the GC flat slab model was greater than that on the NC model. Figure 29 shows the GC-0-F flat slab model had stiffnesses at Time Load 1, 2, 3, 4, 5, and 17 (ultimate) of 554.226 kN/mm, 429.445 kN/mm, 226.510 kN/mm, 62.816 kN/mm, 55.649 kN/mm, and 38.984 kN/mm. At Time Loads 1, 2, 3, 4, 5, and 21 (ultimate), the GC-5-F flat slab model performed stiffnesses of 554.015 kN/mm, 429.074 kN/mm, 231.593 kN/mm, 67.425 kN/mm, 59.153 kN/mm, and 35.528 kN/mm, respectively. The GC-8-F flat slab model exhibited stiffnesses at Time Loads 1, 2, 3, 4, 5, and 18 (ultimate), namely 554.288 kN/mm, 432.545 kN/mm, 254.645 kN/mm, 72.403 kN/mm, 61.975 kN/mm, and 42.934 kN/mm. The GC-8-F flat slab model was more brittle than its GC-5-F counterpart because the transverse reinforcement diameter was larger, resulting in greater stiffness at the same Time Load, while its ultimate Time Load was smaller. Figure 30 shows that

the stiffness degradation at Time Load 1 differs for the flat slab models GC-0-F, GC-5-F, and GC-8-F, namely 11.514%, 11.883%, and 10.564%. Then the stiffness at Time Load 2 decreases to 8.922%, 9.203%, and 8.244% for each flat slab. At the ultimate condition, each GC flat slab model experiences stiffness degradation of 0.810%, 0.762%, and 0.818%.

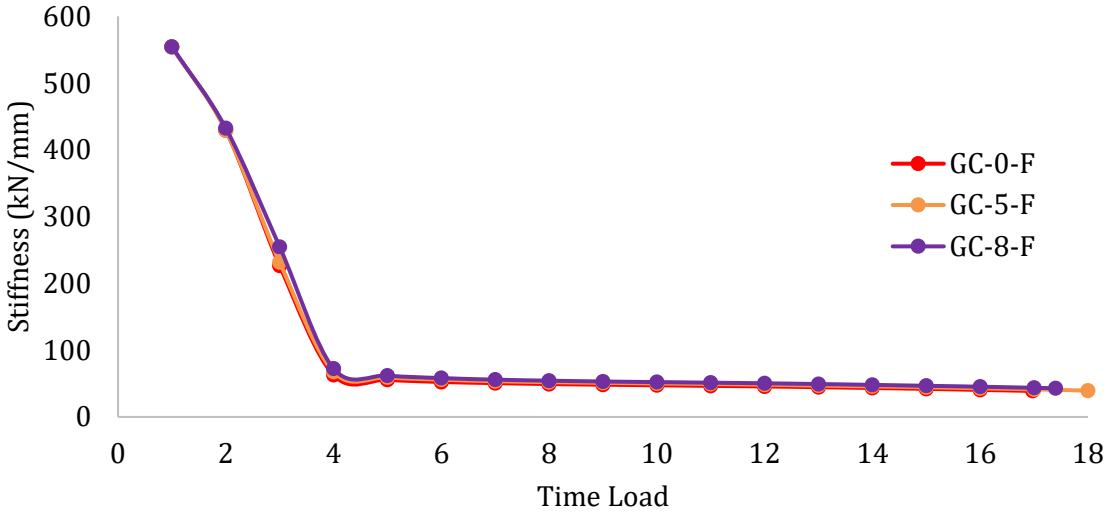

Fig. 29. Curves of stiffness of GC-0-F, GC-5-F, and GC-8-F models

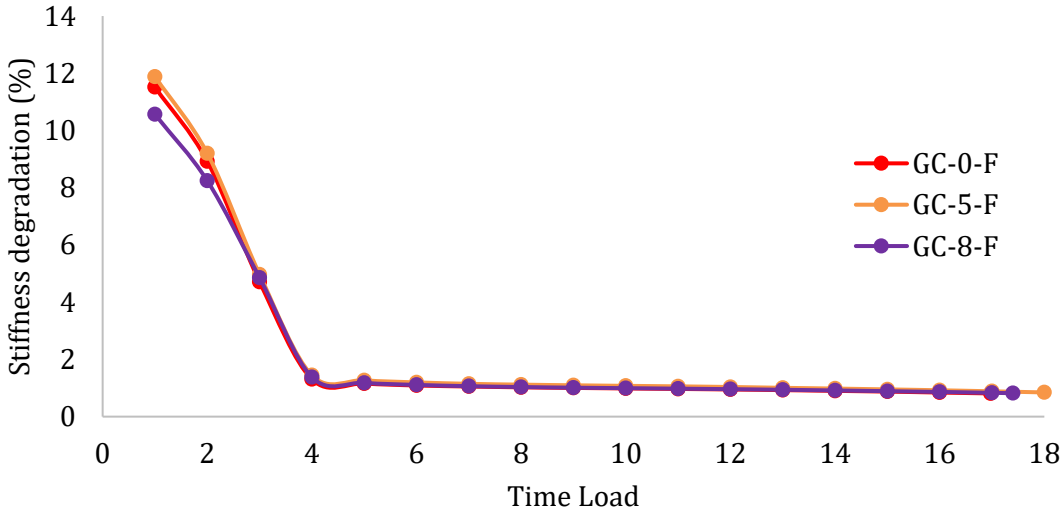

Fig. 30. Curves of stiffness degradation of GC-0-F, GC-5-F, and GC-8-F models

3.12. Energy Absorption of NC and GC Flat Slab Models

Energy absorption is distributed throughout the structure from yielding to ultimate resistance under load. Due to monotonic loading, the amount of energy absorption is calculated from the area of the load-displacement relationship curve from the yielding state to the ultimate state at the end of the loading. Figure 31 depicts the shaded area under the load-displacement curve of the NC-0 flat slab specimen from yield to ultimate state, which is the energy absorption [75]. Similarly, the energy absorption of the NC-5 specimen and the NC-0-F, NC-5-F, and NC-8-F models is presented in Table 9. The unreinforced NC-0-F flat slab model resisted a lower ultimate load than its NC-5-F and NC-8-F counterparts. The NC-5-F model achieved higher ultimate load and displacement than NC-8-F, thereby absorbing the greatest energy among all NC models. The NC-8-F flat slab model was brittle and, therefore, reached a lower ultimate load and displacement than the NC-5-F flat slab model. The difference in energy absorption between the NC-0 specimen and the NC-0-F model is because the NC-0 specimen experiences a greater deflection in the ultimate condition compared to the NC-0 model, with a difference of 1.232 mm or 7.91% as presented in Table 2. It is influenced by the lack of post-cracking tension stiffening or simplified bond behavior in the numerical modeling. The reinforcing steel bars are assumed to be fully bonded to the concrete in all flat slab models.

Thus, the NC-0-F model behaves less ductile than the NC-0 specimen. Table 10 shows that the GC-5-F flat slab model achieved the highest energy absorption at 4727 kN · mm. In comparison, the brittleness of the GC-8-F counterpart reduced its deformation capacity and resulted in a lower energy absorption of 2461.5 kN · mm. Each GC flat slab model absorbed more energy than its NC counterpart with identical transverse reinforcement details. It occurred because GC has a higher compressive strength than NC, allowing the flat slab to resist greater loads under greater displacements.

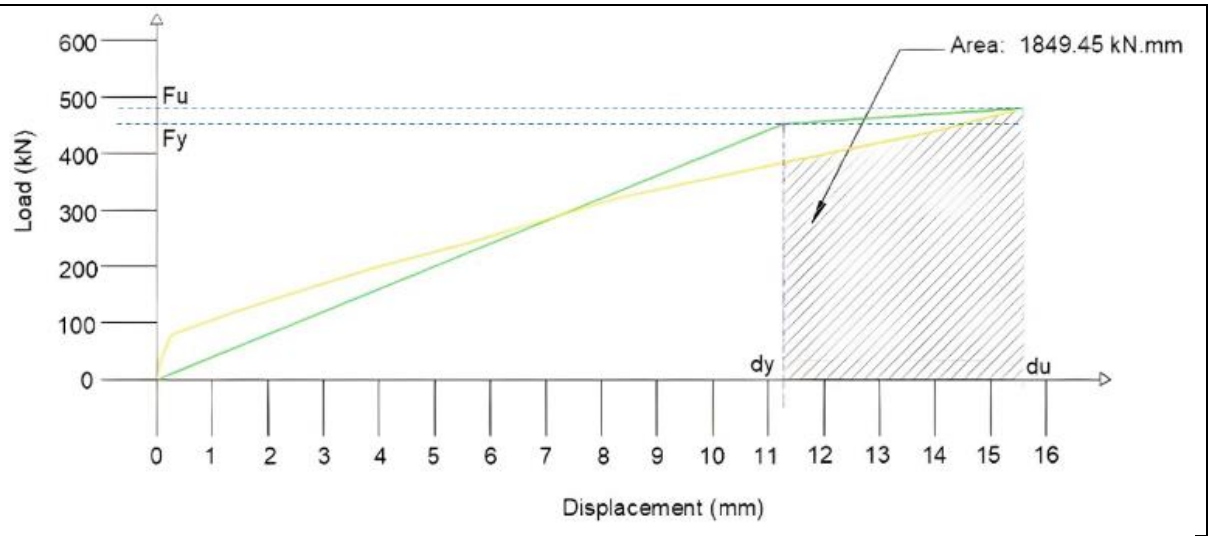

Fig. 31. The shaded area of absorption energy of the NC-0 specimen

Table 9. Energy absorption of the NC flat slab specimens and models

Type of flat slab	Energy absorption of specimen	Type of flat slab	Energy absorption of model	Difference
	(kN · mm)		(kN · mm)	(%)
NC-0	1849.45	NC-0-F	1265.66	31.57
NC-5	3528.37	NC-5-F	3043.95	13.73
NC-8	-	NC-8-F	2437.81	-

Table 10. Energy absorption of the GC flat slab model

Type of flat slab	Energy absorption (model)	Difference with NC model
	(kN · mm)	(%)
GC-0-F	2858.05	125.815
GC-5-F	4727.00	55.292
GC-8-F	2461.50	-

3.13. Punching Shear

The effect of transverse reinforcement is analyzed by examining the nominal shear of each flat slab compared to the resisted shear. Different transverse reinforcement diameters result in various nominal shear strengths and determine the ability to resist punching shear loads. Equations (21)-(34) are used to perform the analysis. The load combination involved in this study is from Table 5.3.1 [17] and expressed by equation (14).

$$W_u = 1.4\ D \tag{21}$$

The critical cross-sectional area for two-way shear on a plate (b_o) is based on Fig. R22.6.4.2a [17] in equation (15). The b_o for all NC and GC flat slabs is 1848 mm.

$$b_o = [(b_{column} + d_{slab}) + (h_{column} + d_{slab})] \times 2 \tag{22}$$

The ultimate shear resisted by the flat slab is given by equation (16).

$$V_u = W_u[L\,W - (b_{column} + d_{slab})] \tag{23}$$

The ultimate factored two-way shear stress around the perimeter of a critical section in Clause 8.4.4.2.1 and the stress of concrete nominal two-way shear strength from Table 22.6.6.1 with shear reinforcement [17] is expressed in equations (24) and (25). The nominal shear stress on steel is given by equation (19).

$$v_u = \frac{V_u}{b_o d_{slab}} \tag{24}$$

$$v_c = 0.17\,\lambda_s \lambda \sqrt{f_c'} \tag{25}$$

$$v_s = \frac{v_u}{\phi} - v_c \tag{26}$$

The size effect factor (λ_s) in Clause 22.5.5.1.3 [17] is written in equation (27).

$$\lambda_s = \sqrt{\frac{2}{1 + 0.004 d_{slab}}} \leq 1 \tag{27}$$

The value of λ for GC is according to Table 19.2.4.1(a) [17] since the density (w_c) of the GC is 2102.9 kg/m^3 [46] and is shown in equation (28). The value of λ for NC is 1 [17]. The required and installed transverse reinforcement area is given by equations (29) and (30).

$$\lambda = 0.0075\,w_c \leq 1.0 \tag{28}$$

$$A_v = \frac{v_s b_o s}{f_{yt}} \tag{29}$$

$$A_v = n\,A_{sv} \tag{30}$$

The nominal shear provided by concrete is expressed in equation (31), based on Clauses 11.11.2.1 [76] and Table 22.6.6.1 [17]. The nominal shear of steel in equation (32) is based on Clauses 11.4.7.2 [76] and 22.6.7.2 [17]. Clause 11.11.7.2 [76] provides equation (33) for nominal shear. Equation (34) shows the strength reduction factor (ϕ), which is 0.75 for shear and adopted from Table 5.3.1 [17].

$$V_c = v_c b_o d = 0.17\,\lambda_s \lambda \sqrt{f_c'} b_o d \tag{31}$$

$$V_s = v_s b_o d = \frac{A_v f_{yt} d}{s} \tag{32}$$

$$V_n = V_c + V_s \tag{33}$$

$$\phi V_n \geq V_u \tag{34}$$

Where; b_o : perimeter of critical section for two-way shear in slabs (mm), b_{column} : width of column cross section (mm); h_{column} : height of column cross section (mm); h_{slab} : height of flat slab = 180 mm (Fig. 2); d_{slab}: effective depth of slab (mm); D: dead load (N); W_u : ultimate load (N) = 1.4 D [17, Table 5.3.1]; V_u : ultimate shear (N); V_c : nominal shear provided by concrete (N); V_s : nominal shear provided by steel (N); L : length of slab (mm) = 2500 mm (Fig. 1); W: width of slab (mm) = 2500 mm (Fig. 1); v_u : factored shear stress (MPa); v_c : nominal shear stress on concrete (MPa); v_s : nominal shear stress on steel (MPa); λ_s : size effect factor; λ: modification factor of the reduced mechanical properties of lightweight concrete to normal weight concrete ; f_c' :compressive strength of concrete (MPa); f_{yt} : yield strength of transverse reinforcement (MPa); w_{NC} : density of NC =

23.50 kN/m³ [77]; w_{GC} : density of GC = 20.62 kN/m³ [46]; q_D : weight of floor finish = 1.5 kN/m² [78, Table 4.3-1]; A_v : total area of transverse reinforcement (mm²); A_{sv} : area of one transverse reinforcement bar (mm²); n: the number of vertical stirrup bars in a cross-section; s: spacing between transverse reinforcement (mm); ϕ_s : diameter of transverse reinforcement (mm)

As an example of calculation using equations (21)-(34), the parameters of the GC-5-F model are described in Appendix. Table 11 presents the shear stresses in flat slabs. The ultimate load on NC and GC flat slabs depended on the concrete density. Thus, the ultimate loads, ultimate shears, ultimate shear stresses, and nominal shear stresses on NC flat slabs were greater than the GC ones. Table 12 shows the flat slab transverse reinforcement. The required transverse reinforcement ($A_{v-required}$) of NC-8 and GC-8 was greater than that of NC-0, NC-5, GC-0, and GC-5 owing to the lesser transverse steel bar yield strength in Table 1. The NC-0 and NC-8 required 68.88 mm² of transverse reinforcement, while the NC-8 required 68.10 mm². The GC flat slabs also show this trend. The GC-0 and GC-5 required 15.34 mm² of transverse reinforcement, while GC-8 required 15.17 mm². The installed transverse reinforcement was 5 mm in diameter for NC-5 and GC-5 flat slabs, while NC-8 and GC-8 flat slabs were installed with 8 mm-diameter transverse reinforcement. The installed transverse reinforcement area is as described in Table 13. These installed steel bars with diameters of 5 mm and 8 mm provided shear stresses of 0.41 MPa and 1.07 MPa, respectively, according to equation (19). Installing transverse reinforcement with an 8 mm diameter, compared to 5 mm, increased shear stress by 2.59 times. The values of λ_s and λ in all NC and GC specimens and models were determined using equations (20) and (21). Thus, the nominal shear stresses provided by the concrete (v_c) were the same for all NC flat slabs, namely 0.93 MPa. Since the reduction factor (ϕ) of 0.75 [17], the obtained ϕv_c is 0.70. In the GC flat slab models, the value of v_c and ϕv_c are 1.10 and 0.82, respectively. The greater area of transverse reinforcement and concrete compressive strength increased the nominal shear stress on the flat slab.

The reduced nominal shear (ϕV_n) of each NC and GC flat slab is compared with the ultimate shear (V_u) to determine its capability in Table 10. Flat slabs without transverse reinforcement, NC-0, NC-0-F, and GC-0-F are unable to resist punching shear because the value of $\phi V_n/V_u$ is less than 1.0, which is 0.72. The NC-5, NC-5-F, and GC-5-F flat slabs can resist punching shear owing to the shear capacity provided by the ϕ5-72 transverse reinforcement. The GC-5-F flat slab shows a higher punching shear capacity with a value of 1.28, compared to its NC-5 and NC-5-F counterparts, which have a value of 1.04. Transverse reinforcement ϕ8-72 increases the punching shear capacity of NC-8 and NC-8-F with a value of 1.55. GC material improves the GC-8-F flat slab's capability, achieving a value of 1.84. Thus, the ϕ5-72 shear reinforcement provides adequate punching shear capacity for NC and GC flat slabs. The transverse reinforcement with a diameter of 8 mm of NC and GC flat slabs provides the highest nominal shear capacity in resisting punching shear. Table 14 shows the increased nominal shear by using GC materials compared with the NC counterparts.

Table 11. Flat slab shear stresses due to ultimate loads

Type of flat slab	Type	W_u (kN)	V_u (kN)	v_u (MPa)	λ_s	λ	ϕv_c (MPa)	v_s (MPa)
NC-0	Specimen	50.14	290.20	0.97	1.00	1.00	0.70	0.36
NC-5	Specimen	50.14	290.20	0.97	1.00	1.00	0.70	0.36
NC-8	Specimen	50.14	290.20	0.97	1.00	1.00	0.70	0.36
NC-0-F	Model	50.14	290.20	0.97	1.00	1.00	0.70	0.36
NC-5-F	Model	50.14	290.20	0.97	1.00	1.00	0.70	0.36
NC-8-F	Model	50.14	290.20	0.97	1.00	1.00	0.70	0.36
GC-0-F	Model	45.61	263.96	0.88	1.00	1.00	0.82	0.08
GC-5-F	Model	45.61	263.96	0.88	1.00	1.00	0.82	0.08
GC-8-F	Model	45.61	263.96	0.88	1.00	1.00	0.82	0.08

Table 12. Flat slab transverse reinforcement

Type of flat slab	Type	$A_{v-required}$	$\phi_{s-required}$	$\phi_{s-installed}$	$A_{v-installed}$	$v_{s-installed}$	Transverse steel bar ratio
		(mm^2)	(mm)	(mm)	(mm^2)	(MPa)	(%)
NC-0	Specimen	68.88	4.68	0	0	0	0
NC-5	Specimen	68.88	4.68	5	78.54	0.41	0.17
NC-8	Specimen	68.10	4.66	8	201.06	1.07	0.44
NC-0-F	Model	68.88	4.68	0	0	0	0
NC-5-F	Model	68.88	4.68	5	78.54	0.41	0.17
NC-8-F	Model	68.10	4.66	8	201.06	1.07	0.44
GC-0-F	Model	15.34	2.21	0	0	0	0
GC-5-F	Model	15.34	2.21	5	78.54	0.41	0.17
GC-8-F	Model	15.17	2.20	8	201.06	1.07	0.44

Table 13. Flat slab nominal shears

Type of flat slab	Type	V_c	V_s	V_n	ϕV_n	$\phi V_n/V_u$
		(kN)	(kN)	(kN)	(kN)	
NC-0	Specimen	278.76	0.00	278.76	209.07	0.72
NC-5	Specimen	278.76	123.35	402.10	301.58	1.04
NC-8	Specimen	278.76	319.39	598.14	448.61	1.55
NC-0-F	Model	278.76	0.00	278.76	209.07	0.72
NC-5-F	Model	278.76	123.35	402.10	301.58	1.04
NC-8-F	Model	278.76	319.39	598.14	448.61	1.55
GC-0-F	Model	327.86	0.00	327.86	245.90	0.93
GC-5-F	Model	327.86	123.35	451.21	338.41	1.28
GC-8-F	Model	327.86	319.39	647.25	485.44	1.84

Table 14. Increase in nominal shears on GC flat slabs

Type of flat slab	Type	Increased V_n (%)
GC-0-F	Model	17.62
GC-5-F	Model	12.21
GC-8-F	Model	8.21

3.14. Mesh Convergence Study

A mesh convergence study was conducted to examine whether the element size affects the flat slab modeling analysis results. The meshing process is performed based on the location of the steel reinforcement, with the side dimensions of the concrete elements ranging from 13 mm to 50 mm. Then, the NC-0-F model element density was increased to ensure that the dimensions of the meshed concrete and steel elements meet accuracy requirements, as shown in Figures 32 and 33. The model identity is NC-0-F-D. The distance between the nodes of NC-0-F-D became closer when compared to NC-0-F in Figures 6 and 7. The side dimensions of the concrete ranged from 13 to 32 mm. The analysis results produced a load-to-deflection curve in Figure 34. It shows that the NC-0-F-D model curve almost coincides with the NC-0-F curve. This indicates that the element size in NC-0-F was sufficient to produce an accurate finite element analysis.

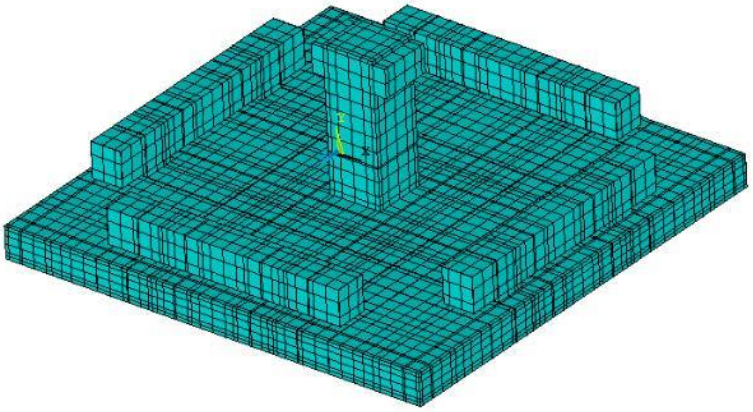

Fig. 32. The top side of a flat slab NC-0-F-D model

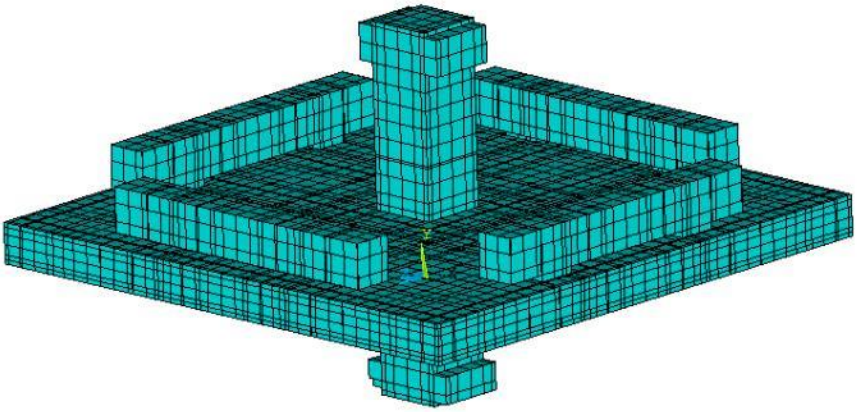

Fig. 33. Three-dimensional side view of the flat slab NC-0-F-D model

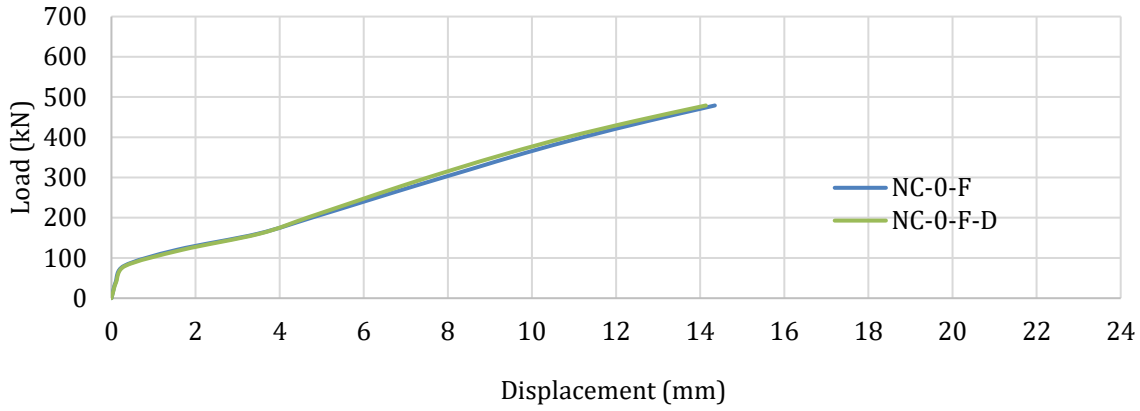

Fig. 34. Comparison of load-deflection curves of NC-0-F and NC-0-F-D

3.15. Limitations and Future Works

In this study, the elaboration and analysis of the NC and GC flat slab numerical models are still limited to the following points:

- The GC behavior was not experimentally validated.
- Only two bar diameters (5 mm and 8 mm) and one spacing (72 mm) were studied for finite element modeling.
- The unbalanced moments at slab-column connections and long-term durability effects were not considered.
- No crack patterns were produced from the finite element modeling.
- Numerical modeling is still limited in simulating post-yield energy absorption, which is influenced by stiffness and ultimate capacity.

- The broader significance of the novelty of this study remains underdeveloped.

The suggestions for future work to improve the quality of the analysis results are as follows:

- Experimental works to validate the numerical findings, especially for NC-8 and all GC flat slab models.
- Further study of the effect of transverse reinforcement ratio on flat slab ductility.

4. Conclusions

The NC-0-F and NC-5-F flat slab numerical models, developed in ANSYS, were verified against specimens and met the accuracy requirements. The performance of the NC flat slab specimens and models, as well as the GC flat slab models, was analyzed, including ultimate loads, displacements, ductility ratios, stress contours, displacement contours, stiffness, energy absorption, and shear capacity. Some conclusions are elaborated as follows.

- The NC-0 and NC-5 flat slab specimens were modelled using the finite element method and verified. The NC-0-F model shows a displacement difference of 7.909% compared with the NC-0 specimen. The NC-5-F model performed a displacement discrepancy of 1.563% compared with the NC-5 specimen. These percentages meet the 10% accuracy limit.
- The percentage of transverse reinforcement significantly affected the shear resistance capacity of a flat slab. In all NC flat slab specimens and models, the highest transverse reinforcement percentage of 0.44% resulted in the flat slab's ability to withstand the best punching shear. The NC-8-F flat slab model achieved the best shear of 616 kN. However, the influence of excessive transverse reinforcement at 0.44% in the GC-8-F flat slab model led to brittle behavior, reduced ductility, and limited deformation capacity. Thus, the GC-8-F flat slab model achieved less ultimate shear and displacement (696 kN; 16.211 mm) than the GC-5-F counterpart (805 kN; 22.658 mm). It indicated that the higher compressive strength of GC than that of NC led to less ductility. Thus, the ultimate displacement and shear of the GC-8-F flat slab model were not as high as those of the GC-5-F counterpart. Each GC flat slab model achieved a higher ultimate shear than the NC models with the same transverse reinforcement ratio. It was owing to the greater compressive strength and elastic modulus of the GC than those of the NC, namely 41.5 MPa and 30266 MPa for the GC, and 30 MPa and 22500 MPa for the NC, respectively.
- The stress contour of the NC-0-F flat slab model shows increasingly higher compressive stresses of 3-12 MPa in the slab around the columns. The portion of the slab under compressive stresses of 12-21 MPa is wider in the NC-5-F and NC-8-F flat slab models than in the NC-0-F model, due to the higher ultimate shear strength. The GC flat slab models exhibit higher and wider compressive stresses of 1.08-17.23 MPa compared to the NC flat slab models (3-12 MPa). The largest compressive stress area occurs in the GC-5-F flat slab model, due to the highest ultimate shear among the models.
- The displacement contour of the NC-0-F flat slab model shows that larger vertical displacements occur in the spreader beams (11.64-14.61 mm). The larger vertical displacements occur at the edges and corners of the NC-5-F and NC-8-F flat slab models (17.58-26.50 mm). In the GC-0-F and GC-5-F flat slab models, larger vertical displacements occur at the flat slab edges and corners, ranging from 13.86 to 31.50 mm. In contrast, the vertical displacement in the GC-8-F (13.86-24.44 mm) is not as large as in the GC-5-F flat slab due to its more brittle behavior, which originates from the largest area of transverse reinforcement.
- The compressive strength of NC and GC, as well as the area of transverse reinforcement, affects ductility. Each GC flat slab model has a higher ductility ratio than its NC counterpart, owing to GC's compressive strength, which enables higher ultimate loads and displacements. The larger areas of transverse reinforcement in NC-8-F and GC-8-F result in lower ductility ratios (1.283 and 1.309) than in NC-5-F and GC-5-F flat slab models (1.380 and 1.390). The NC-0-F and GC-0-F flat slab models without transverse reinforcement are unable to withstand significant ultimate shear and displacement, resulting in low ductility ratios (1.248 and 1.359).

- The stiffness of the NC and GC specimens and models decreased drastically from Time Load 1 to 4 due to widespread element damage at the beginning of monotonic loading. From Time Load 5 to the final load, stiffness degradation occurred slowly, owing to a slower reduction in shear capacity after yield. The stiffnesses of NC-0-F, NC-5-F, and NC-8-F at Time load 1 were 396,660 kN/mm, 396.888 kN/mm, and 397.164 kN/mm, respectively. Then on Time Load 4, they were 46,059 kN/mm, 51.074 kN/mm, and 52.469 kN/mm. While the stiffnesses of GC-0-F, GC-5-F, and GC-8-F at Time load 1 were 554.226 kN/mm, 554.015 kN/mm, and 554.288 kN/mm. At Time Load 4, the stiffnesses were 62.816 kN/mm, 67.425 kN/mm, and 72.403 kN/mm, respectively.
- The energy absorption of GC flat slab models is higher than that of NC counterparts. The GC-5-F flat slab model absorbs the highest energy of all models at 4727 kN · mm. The significant difference in energy absorption indicates that the GC material can improve the performance of flat slabs compared to the NC ones.
- The GC material increases the nominal punching shear, as shown by all GC flat slab models, compared with the NC counterparts. The increment of nominal punching shear on GC-0-F, GC-5-F, and GC-8-F are 17.62%, 12.21%, and 8.21%, respectively. The ultimate shear can be overcome by the presence of $\phi 5 - 72$ as the minimum adequate transverse reinforcement in the GC and NC flat slabs. All flat slabs without transverse reinforcement are unable to withstand the punching shear since the $\phi V_n/V_u$ values are less than 1.0.
- The use of transverse reinforcement in flat slabs needs to consider the influence of the concrete material properties to produce structural members that provide sufficient punching shear and ductility capabilities. These results of this study could inform design practice or future experimental validation.

Acknowledgement

The authors would like to thank Sriwijaya University for providing facilities and support for this research activity.

Appendix

The data used in this study for numerical modeling are summarized in Table A.

Table A. Numerical model parameters

Parameter	Data	Location
Type of elements	Concrete: three-dimensional SOLID65 discrete element with 8 nodes (8-node brick elements). Steel bar: 2-nodes LINK180 discrete bar elements.	2.2.1 Concrete Element Paragraph #1 2.2.2 Steel Bar Element Paragraph #1
Concrete properties	NC: f_c' = 30 MPa E_c = 22500 MPa GC: f_c' = 41.5 MPa E_c = 30266 MPa	2.1. Details of Specimens and Models Paragraph #1-2
Steel properties including tensile strength	f_{yl} and f_{yt}	Table 1. Steel bars properties
Fracture energy	NC: G_f = 64.73 N.m/mm^2 GC: G_f = 67.70 N.m/mm^2	2.3. Material Properties Paragraph #2

Parameter	Data	Location
Poisson's ratio	NC: ν = 0.20 GC: ν = 0.22	2.3. Material Properties Paragraph #1 The Poisson's ratios of NC and GC are assumed to be 0.2 [53] and 0.22 [54], respectively.
Bond assumptions	The reinforcing steel is assumed to be fully bonded to the concrete.	2.2.2 Steel Bar Element Paragraph #1
Mesh size	NC-0-F, NC-5-F, NC-8-F, GC-0-F, GC-5-F, GC-8-F models: 13 mm to 50 mm. NC-0-F-D model: 13 to 32 mm.	3.14. Mesh Convergence Study Paragraph #1

Example of calculation using equations (14)-(27) for the GC-5-F model:

- b_{column} : 300 mm (2.1. Details of Specimens and Models; paragraph #2)
- h_{column} : 300 mm (2.1. Details of Specimens and Models; paragraph #2)
- d_{slab} : 162 mm (2.1. Details of Specimens and Models; paragraph #2)
- $s = 72$ mm (Fig. 2)
- $L = 2.5$ m; $W = 2.5$ m (Fig. 1)
- Thickness of the flat slab: $h_{fs} = 180$ mm (Fig. 2)
- $n = 4$ (Fig. 4)
- $f_{yt} = 698$ MPa (Table 1)
- Density of GC: $w_{GC} = 2102.9$ kg/m^3 [46] = 20.62 kN/m^3
- Self-weight of the flat slab: $SW_{fl} = h_{fs} w_{GC} LW = 23.20$ kN
- Weight of floor finish = 1.5 kN/m^2 (assumed)
- Weight of floor finish on the flat slab: w_f = Weight of floor finish × L × W = 9.38 kN
- Dead Load: $D = w_{GC} + w_f = 32.57$ kN

$$W_u = 1.4\, D = 45.61\ kN \tag{21}$$

$$b_o = [(b_{column} + d_{slab}) + (h_{column} + d_{slab})] \times 2 = 1848 \text{ mm} \tag{22}$$

$$V_u = W_u[L\, W - (b_{column} + d_{slab})] = 263.96 \text{ kN} \tag{23}$$

$$v_u = \frac{V_u}{b_o d_{slab}} = 0.88 \text{ MPa} \tag{24}$$

$$v_c = 0.17\, \lambda_s \lambda \sqrt{f_c'} = 1.10 \text{ MPa} \tag{25}$$

$$v_s = \frac{v_u}{\phi} - v_c = 0.08 \text{ MPa} \tag{26}$$

$$\lambda_s = \sqrt{\frac{2}{1+0.004 d_{slab}}} \leq 1; \text{ then } \lambda_s = 1 \tag{27}$$

$$\lambda = 0.0075\, w_c \leq 1.0; \text{ then } \lambda_{GC} = 1 \tag{28}$$

$$A_v = \frac{v_s b_o s}{f_{yt}} = 15.34 \text{ mm}^2\ (= A_{v-required}) \tag{29}$$

$$A_v = n\, A_{sv} = n\left(0.25\pi {\phi_s}^2\right) = 78.54 \text{ mm}^2\ (= A_{v-installed}) \tag{30}$$

$$V_c = v_c b_o d = 0.17\, \lambda_s \lambda \sqrt{f_c'} b_o d = 327.86 \text{ kN} \tag{31}$$

$$V_s = v_s b_o d = \frac{A_v f_{yt} d}{s} = 123.35 \text{ kN} \tag{32}$$

$$V_n = V_c + V_s = 451.21 \text{ kN} \tag{33}$$

$$\phi V_n \geq V_u \text{ then } 338.41 \text{ kN} \geq 263.96 \text{ kN} \tag{34}$$

References

[1] Sundararaj JB, Rajkumar KPR. Effects of multiple precursors on strength, durability, and microstructural properties of ambiently cured geopolymer concrete. Construction and Building Materials, 2024; 442; 137538. https://doi.org/10.1016/j.conbuildmat.2024.137538

[2] Deep A, Sarkar P. Enhancing sustainability in concrete construction: Utilizing copper slag for improved properties of geopolymer concrete. Construction and Building Materials, 2024; 453; 1390442024. https://doi.org/10.1016/j.conbuildmat.2024.139044

[3] Kanagaraj B, Raj RS, Anand N, Lubloy E. Engineering and sustainability performance of geopolymer concrete blended with sodium silicate effluent. Developments in the Built Environment, 2025; 22; 100678. https://doi.org/10.1016/j.dibe.2025.100678

[4] Abdalla JA, Hawileh RA, Bahurudeen A, Jyothsna G, Sofi A, Shanmugam V, Thomas BS. A comprehensive review on the use of natural fibers in cement/geopolymer concrete: A step towards sustainability. Case Studies in Construction Materials, 2023; 19; e02244. https://doi.org/10.1016/j.cscm.2023.e02244

[5] Yan G, Hu J, Chen M, Ma Y, Huang H, Zhang Z, Wei J, Shi C, Yu Q. Performance evaluation of reinforced slag-fly ash-ceramic waste powders ternary geopolymer concrete under chloride ingress environment. Construction and Building Materials, 2025; 478; 141447. https://doi.org/10.1016/j.conbuildmat.2025.141447

[6] Wang W, Zhang P, Dai X, Zheng Y, Hu S. Workability of self-compacting geopolymer concrete: The effect of nano-SiO2 and steel-polyvinyl alcohol hybrid fiber. Construction and Building Materials, 2025; 460; 139849. https://doi.org/10.1016/j.conbuildmat.2024.139849

[7] Jaji MB, Babafemi AJ, Zijl GPAG. Mechanical performance of extrusion-based two-part 3D-printed geopolymer concrete: A review of advances in laboratory and real-scale construction projects. Materials Today Sustainability, 2025; 31; 101131. https://doi.org/10.1016/j.mtsust.2025.101131

[8] Ozkilic YO, Celik AI, Tunc U, Karalar M, Deifalla A, Alomayri T, Althoey F. The use of crushed recycled glass for alkali activated fly ash based geopolymer concrete and prediction of its capacity. Journal of materials research and technology, 2023; 24: 8267-8281. https://doi.org/10.1016/j.jmrt.2023.05.079

[9] Kishore K, Sheikh MN, Hadi, MNS. Functionalization of carbon nanotubes for enhanced dispersion and improved properties of geopolymer concrete: A review. Journal of Building Engineering, 2025; 111; 113096. https://doi.org/10.1016/j.jobe.2025.113096

[10] Murali G. Recent research in mechanical properties of geopolymer-based ultrahigh-performance concrete: A review. Defence Technology, 2024; 32; 67e88. https://doi.org/10.1016/j.dt.2023.07.003

[11] Ahmed F, Biswas RK, Ahsan KA, Islam S, Rahman MR. Estimation of strength properties of geopolymer concrete. Materials Today: Proceedings, 2021; 44: 871-877. https://doi.org/10.1016/j.matpr.2020.10.790

[12] Akduman S, Aktepe R, Aldemir A, Ozcelikci E, Alam B, Sahmaran M. Opportunities and challenges in constructing a demountable precast building using C&D waste-based geopolymer concrete: A case study in Türkiye. Journal of Cleaner Production, 2024; 434; 139976. https://doi.org/10.1016/j.jclepro.2023.139976

[13] Zadjelovic V, Wright RJ, Walker TR, Avalos V, Marín PE, Christie-Oleza JA, Riquelme C. Assessing the impact of chronic and acute plastic pollution from construction activities and other anthropogenic sources: A case study from the coast of Antofagasta, Chile. Marine Pollution Bulletin, 2023; 195; 115510. https://doi.org/10.1016/j.marpolbul.2023.115510

[14] Adufu YD, Sore SO, Nshimiyimana P, Ahouandjinou KD, Messan A, Escadeillas G. Durability behaviors of calcined kaolin clay-based geopolymer concrete containing different calcium compounds and cured in ambient sub-Saharan climate. Construction and Building Materials, 2025; 465; 140195. https://doi.org/10.1016/j.conbuildmat.2025.140195

[15] Dehkordi ER, Ramezanianpour AA, Moodi F. Application of pre-fabricated geopolymer permanent formworks (PGPFs): A novel approach to provide durability and mechanical strength of reinforced concrete. Journal of Building Engineering, 2022; 45; 103517. https://doi.org/10.1016/j.jobe.2021.103517

[16] Kanagaraj B, Raj SR, Anand N, Lubloy E. Fire performance of concrete: A comparative study between cement concrete and geopolymer concrete & its application - A state of art-review. Case Studies in Chemical and Environmental Engineering, 2025; 11; 101212. https://doi.org/10.1016/j.cscee.2025.101212

[17] American Concrete Institute. ACI CODE-318-25: Building Code for Structural Concrete - Code Requirements and Commentary, Farmington Hills, American Concrete Institute, 2025.

[18] The National Standardization Agency. SNI 2847:2019 Structural Concrete Requirements for Buildings and Explanation. Jakarta: The National Standardization Agency, 2019. (in Indonesian)

[19] Chen Z, Tang J, Wang Y, Yi C, Su T. Characterizing the interfacial bonding behaviour and influential mechanism of metakaolin-based geopolymer-concrete composites under shearing load: Experimental

and modelling study. Composite Structures, 2025; 369; 119336. https://doi.org/10.1016/j.compstruct.2025.119336
[20] Alameri M, Ali MSM, Sheikh A, Elchalakani M. Investigation of high-performance geopolymer concrete-filled double-skin columns under combined loading conditions. Journal of Constructional Steel Research, 2025; 229; 109523. https://doi.org/10.1016/j.jcsr.2025.109523
[21] Kumar TU, Kumar MV, Lakkaboyana SK, Trilaksana H, Ansari A. Investigation of bond strength and flexural behaviour of geopolymer aggregate concrete beams. Case Studies in Construction Materials, 2025; 22; e04916. https://doi.org/10.1016/j.cscm.2025.e04916
[22] Huang Y, Grünewald S, Schlangen E, Lukovic M. Strengthening of concrete structures with ultra high performance fiber reinforced concrete (UHPFRC): A critical review. Construction and Building Materials, 2022; 336; 127398. https://doi.org/10.1016/j.conbuildmat.2022.127398
[23] Li Z, Guo Y, Rao S, Shang X, Noori M, Altabey WA, Farsangi EN, Zhu H, Liu P. On the investigation of modular high-rise concrete buildings in the Asia Pacific region: Engineering application analysis and future directions. Results in Engineering, 2025; 26; 104830. https://doi.org/10.1016/j.rineng.2025.104830
[24] Guo Y-C, Cai Y-J, Xie Z-H, Xiao S-H, Zhuo K-X, Cai P-D, Lin J-X. Experimental investigation of GFRP bar bonding in geopolymer concrete using hinged beam tests. Engineering Structures, 2025; 322; 119036. https://doi.org/10.1016/j.engstruct.2024.119036
[25] Wan S, Zong Z, Lin Y, Shi H, Yuan Y, Ding B, Cai J. Shear behavior of reinforced one-part geopolymer concrete beams. Journal of Building Engineering, 2025; 111; 113205. https://doi.org/10.1016/j.jobe.2025.113205
[26] Li Y, Wei J, Han A, Xu Y, Qiao M, He D. Influence of geopolymer foam concrete on the mechanical performance of cold-formed steel built-up columns. Case Studies in Construction Materials, 2025; 22; e04479. https://doi.org/10.1016/j.cscm.2025.e04479
[27] Özbayrak A, Kucukgoncu H, Aslanbay YG, Aslanbay HH. Experimental and Numerical Analysis of Damage and Crack Behavior in Geopolymer and Ordinary Portland Cement Reinforced Concrete Columns. Journal of Building Engineering, 2025; 111; 113623. https://doi.org/10.1016/j.jobe.2025.113623
[28] Tiwary AK, Singh H, Singh K, Sharma A. Experimental and analytical performance analysis of geopolymer concrete-filled double steel tube (CFDST) columns under axial loading. Structures, 2025; 74; 108572. https://doi.org/10.1016/j.istruc.2025.108572
[29] Coronelli D, Muttoni A, Martinelli L, Vecchio CD, d'Aragona MG, Lignola GP, Prota A, Kagermanov A, Marinkovic M. Flat slab response for seismic and cyclic actions prediction with numerical models. Engineering Structures, 2023; 289; 116307. https://doi.org/10.1016/j.engstruct.2023.116307
[30] Sîli AA. Earthquake behavior of flat slab structures, particularities and opportunities for use in the building stock of the Chisinau municipality. IOP Conference Series: Materials Science and Engineering, 2024; 1304; 012010. https://doi.org/10.1088/1757-899X/1304/1/012010
[31] Hawkins NM, Fallsen HB, Hinojosa RC. Influence of Column Rectangularity on the Behavior of Flat Plate Structures. Cracking, Deflection and Ultimate Load of Concrete Slab Systems, SP-30, American Concrete Institute Journal & Proceedings, 1972; 69(1): 68-87, Farmington Hills, MI.
[32] Akinpelu MA, Gabriel DS, Salman AM, Raheem IA. Numerical study on the effect of different column shapes on punching shear behavior of flat slabs. Results in Engineering, 2023; 19, 101345. https://doi.org/10.1016/j.rineng.2023.101345
[33] El-Kassas AI, Bashandy AA, Eied FAM, Arab MAES. Effect of fibers type on the behavior of fibrous high-strength self-compacted reinforced concrete flat slabs in punching with and without shear reinforcement. Construction and Building Materials, 2022; 360; 129625. https://doi.org/10.1016/j.conbuildmat.2022.129625
[34] Santos JB, Melo GdS, Ruiz MF. Punching performance of flat slabs with openings accounting for the influence of moment transfer and shear reinforcement. Engineering Structures, 2024; 303; 117461. https://doi.org/10.1016/j.engstruct.2024.117461
[35] Zufarihsan R, Tambusay A, Suryanto B, Suprobo P. Predicting the punching failure of lightly reinforced concrete flat slabs without shear reinforcement. Structures, 2025; 74; 108473. https://doi.org/10.1016/j.istruc.2025.108473
[36] Ghalla M, Mansour W, Li W, Wang P, Badawi M, Zareef MAE. Enhancing the punching performance of two-way RC flat slabs using different configurations of embedded aluminum sections: Experimental program and numerical analysis. Construction and Building Materials, 2024; 434; 136737. https://doi.org/10.1016/j.conbuildmat.2024.136737
[37] Edri IE, Yankelevsky DZ. Numerical framework for assessing punching shear behavior inintegrity-reinforced concrete flat slab specimens. Structures, 2025; 76; 108823. https://doi.org/10.1016/j.istruc.2025.108823

[38] Nguyen-The D, Thai S, Nguyen-Van H, Ngo-Huu C. Numerical modelling of punching shear behaviour of reinforced concrete flat slab and CFT column connections using steel plates. Structures, 2025; 74; 108594. https://doi.org/10.1016/j.istruc.2025.108594
[39] Lim S, Kim M, Lee J-Y, Kim H, Kim D, Jo M, Kim K. Punching shear strength of RC flat plate slab-column connections strengthened with column head steel plates. Journal of Building Engineering, 2025; 111; 113132. https://doi.org/10.1016/j.jobe.2025.113132
[40] Zhou Y, Shou H, Li C, Jiang Y, Tian X. Punching shear behavior of ultra-high-performance fiber-reinforced concrete and normal strength concrete composite flat slabs. Engineering Structures, 2025; 322; 119123. https://doi.org/10.1016/j.engstruct.2024.119123
[41] Lima H, Palhares R, Melo G Sd, Oliveira M. Experimental analysis of punching shear in flat slabs with variation in the anchorage of shear reinforcement. Structural Concrete, 2020; 22(2): 1165-1182. https://doi.org/10.1002/suco.202000158
[42] Aguiar A, Oliveira D, Reis L, Nzambi A. Punching shear strength of waffle flat slabs with opening adjacent to elongated columns. Engineering Structures, 2021; 243; 112641. https://doi.org/10.1016/j.engstruct.2021.112641
[43] Arief A, Nurjannah SA, Megantara Y, Rusli M, Putra FE, Noviyanto A. Experimental study of confined masonry walls with lap splice reinforcement subjected to cyclic loads. Engineering Structures, 2024; 301; 117247. https://doi.org/10.1016/j.engstruct.2023.117247
[44] Saloma, Nurjannah SA, Usman AP, Aminuddin KM, Iqbal MM, Rifkah. Shear Capacity of Geopolymer Concrete Deep Beams with Variation of Transverse Reinforcement Ratio. Civil Engineering and Architecture, 2024; 12(1): 293-311. https://doi.org/10.13189/cea.2024.120123
[45] Saloma, Nurjannah SA, Hanafiah, Usman AP, Hu S, Usman F. Behavior of Geopolymer Concrete Wall Panels with Square Opening Variations Subjected to Cyclic Loads. Journal of Applied Engineering Science, 2023; 21(3), 1130: 884-895. https://doi.org/10.5937/jaes0-43777
[46] Zulfiati R, Saloma, Idris Y. Mechanical properties of fly ash-based geopolymer with natural fiber. IOP Conference Series: Journal of Physics, 2019; 1198, 082021. https://doi.org/10.1088/1742-6596/1198/8/082021
[47] Wu H, Zhuang X, Zhang W, Zhao Z. Anisotropic ductile fracture: Experiments, modeling, and numerical simulations. Journal of Materials Research and Technology, 2022; 20: 833-856. https://doi.org/10.1016/j.jmrt.2022.07.128
[48] Badshah M, Badshah S, Jan S. Comparison of Computational Fluid Dynamics and Fluid Structure Interaction Models for The Performance Prediction of Tidal Current Turbines. Journal of Ocean Engineering and Science, 2020; 5: 164-172. https://doi.org/10.1016/j.joes.2019.10.001
[49] https://ansyshelp.ansys.com/public/account/secured?returnurl=/Views/Secured/main_page.html. (accessed on October 30, 2025)
[50] Al-Murshidi KR, Al-Ta'ee KN, Al-Janabi MA. Finite element analysis of cellular circle cofferdam for wet soil. Kufa Journal of Engineering, 2014; 6(1): 25-44. https://doi.org/10.30572/2018/KJE/611310
[51] Özbayrak A, Kucukgoncu H, Atas O, Aslanbay HH, Aslanbay YG, Altun F. Determination of stress-strain relationship based on alkali activator ratios in geopolymer concretes and development of empirical formulations. Structures, 2023; 48: 2048-2061. https://doi.org/10.1016/j.istruc.2023.01.104
[52] The European Union Per Regulation 305/2011. EN 1992-1-1 Eurocode 2: Design of concrete structures - Part 1-1: General rules and rules for buildings. 2004.
[53] Ayeni IS, Lim NHAS, Samad M. Engineering properties of natural fibre-reinforced one-part geopolymer concrete. Construction and Building Materials, 2024; 456, 139161. https://doi.org/10.1016/j.conbuildmat.2024.139161
[54] CEB-FIP. Comit'e Euro-International du B'eton (CEB-FIP Model Code 1990). 1993, London: Thomas Telford Ltd.
[55] Mohamed O, Khattab R. Effect of Shear Reinforcement on Punching Shear Capacity of Reinforced Concrete Flat Plates. IOP Conference Series: Materials Science and Engineering, 2020; 960; 042077. https://doi.org/10.1088/1757-899X/960/4/042077
[56] Xiangyong N, Bin Z, Yizhu L, Yonghui H. Predicted compressive stress-strain model for high-strength stirrup confined concrete. Structures, 2023; 52: 933-945. https://doi.org/10.1016/j.istruc.2023.04.039
[57] Alex AG, Gebrehiwet T, Kemal Z, Subramanian RB. Structural Performance of Low-Calcium Fly Ash Geo-polymer Reinforced Concrete Beam. Iranian Journal of Science and Technology, Transactions of Civil Engineering, 2022. https://doi.org/10.1007/s40996-022-00832-x
[58] Öz HÖ, Yücel HE, Günes M, Köker TS. Fly-ash-based geopolymer composites incorporating cold-bonded lightweight fly ash aggregates. Construction and Building Materials, 2021; 272, 121963. https://doi.org/10.1016/j.conbuildmat.2020.121963
[59] Jiang H, Fang Z, Liu A, Li Y, Feng J. Interface shear behavior between highstrength precast girders and lightweight cast-in-place slabs. Construction and Building Materials, 2016; 128: 449-460. https://doi.org/10.1016/j.conbuildmat.2016.10.088

[60] Purwanto, Ekaputri JJ, Nuroji, Indriyantho BR, Han A, Gan BS. Shear-bond behavior of self-compacting geopolymer concrete to conventional concrete. Construction and Building Materials, 2022; 321, 126167. https://doi.org/10.1016/j.conbuildmat.2021.126167
[61] Shibayama A, Nishiyama M. Shear strength of reinforced fly-ash-based geopolymer concrete beams with and without shear reinforcement. Structures, 2023; 50: 603-614. https://doi.org/10.1016/j.istruc.2023.02.060
[62] Kuo WT, Liu MY, Juang CU. Bonding behavior of repair material using flyash/ground granulated blast furnace slag-based geopolymer. Materials, 2019; 12(10), 1697. https://doi.org/10.3390/ma12101697
[63] Zailani WWA, Bouaissi A, Abdullah MMAB, Razak RA, Yoriya S, Salleh MAAM, Rozainy MR, Fansuri H. Bonding Strength Characteristics of FA-Based Geopolymer Paste as a Repair Material When Applied on OPC Substrate. Applied Sciences, 2020; 10 (9), 3321. https://doi.org/10.3390/app10093321
[64] Ganeshan M, Venkataraman S. Interface shear strength evaluation of self compacting geopolymer concrete using push-off test. Journal of King Saud University - Engineering Sciences, 2020; 34: 98-107. https://doi.org/10.1016/j.jksues.2020.08.005
[65] Topark-Ngarm P, Chindaprasirt P, Sata V, Setting time, strength, and bond of high-calcium fly ash geopolymer concrete. Journal of Materials in Civil Engineering; 2015, 04014198. https://doi.org/10.1061/(ASCE)MT.1943-5533.0001157
[66] Phoo-Ngernkham T, Hanjitsuwan S, Li L-Y, Damrongwiriyanupap N, Chindaprasirt P. Adhesion characterisation of portland cement concrete and alkaliactivated binders. Advances in Cement Research, 2019; 31(2): 69-79. https://doi.org/10.1680/jadcr.17.00122
[67] Meesala CR, Verma NK, Kumar S. Critical review on fly-ash based geopolymer concrete. Structural Concrete, 2020; 21(3): 1013-1028. https://doi.org/10.1002/suco.201900326
[68] Hassan A, Arif M, Shariq M. A review of properties and behaviour of reinforced geopolymer concrete structural elements-a clean technology option for sustainable development. Journal of Cleaner Production, 2020; 245, 118762. https://doi.org/10.1016/j.jclepro.2019.118762
[69] Phoo-Ngernkham T, Hanjitsuwan S, Detphan S, Thumrongvut J, Suksiripattanapong C, Damrongwiriyanupap N, Chindaprasirt P, Hatanaka S. Shear bond strength of FA-pc geopoylmer under different sand to binder ratios and sodium hydroxide concentrations. International Journal of GEOMATE, 2018; 14(42): 52-57. DOI: 10.21660/2018.42.7152. https://doi.org/10.21660/2018.42.7152
[70] Qian K, Liu J-G, Yu X-H, Weng Y-H. Experimental and numerical investigation of punching shear capacity of corroded reinforced concrete slab-column connections. Structures, 2022; 43: 1548-1557. https://doi.org/10.1016/j.istruc.2022.07.065
[71] Nurjannah SA, Saloma, Aminuddin KM, Usman AP, Saggaff A, Muliawan RA, Ngian SP. Performance of Cold-Formed Steel Beam-Column Joint with Variation in Haunched Gusset Plate Length Subjected to Monotonic Loads. Civil Engineering and Architecture, 2025; 13(4): 2922-2944. https://doi.org/10.13189/cea.2025.130409
[72] Thomas P, Priestley MJN. Seismic Design of Reinforced Concrete and Masonry Buildings. Wiley & Sons, Incorporated, John, Oxford, 1992.
[73] Federal Emergency Management Agency (FEMA). FEMA 356. Prestandard and Commentary for The Seismic Rehabilitation of Buildings. Washington DC: FEMA, 2000.
[74] Gilbert RI, Sakka ZI. Strength and ductility of reinforced concrete slabs containing welded wire fabric and subjected to support settlement. Engineering Structures, 2010, 32: 1509-1521. https://doi.org/10.1016/j.engstruct.2010.01.025
[75] Decanini L. Estimation of Near-Source Ground Motion and Seismic Behaviour of RC Framed Structures Damaged by the 1999 Athens Earthquake. Journal of Earthquake Engineering, 2005; 9(5): 609-635. https://doi.org/10.1080/13632460509350559
[76] American Concrete Institute. ACI CODE-318-08: Building Code for Structural Concrete - Code Requirements and Commentary, Farmington Hills, American Concrete Institute, 2008.
[77] Ashraf M. ACI SP-17M(14) The Reinforced Concrete Design Handbook: A Companion to ACI 318M-14. 218, American Concrete Institute.
[78] American Society of Civil Engineers (ASCE). ASCE/SEI 7-22 Minimum Design Loads and Associated Criteria for Buildings and Other Structures, 2022, Structural Engineering Institute.